Supplementary Information for:

Double-Stranded RNA under Force and Torque: Similarities to and Striking Differences from Double-Stranded DNA

Jan Lipfert[a,b], Gary M. Skinner[a,1], Johannes M. Keegstra[a,2], Toivo Hensgens[a], Tessa Jager[a], David Dulin[a], Mariana Köber[a], Zhongbo Yu[a], Serge P. Donkers[a], Fang-Chieh Chou[c], Rhiju Das[c,d], and Nynke H. Dekker[a,3]

[a]Department of Bionanoscience, Kavli Institute of Nanoscience, Delft University of Technology, Lorentzweg 1, 2628 CJ Delft, The Netherlands

[b]Department of Physics, Nanosystems Initiative Munich, and Center for NanoScience (CeNS), Ludwig-Maximilians-University Munich, Amalienstrasse 54, 80799 Munich, Germany

[c]Departments of Biochemistry and [d]Physics, Stanford University, Stanford, CA 94305, USA

[1]Present address:
Illumina UK, Chesterford Research Park, Little Chesterford, Essex, CB10 1XL, United Kingdom

[2]Present address:
FOM Institute for Atomic and Molecular Physics (AMOLF), Science Park 104, 1098 XG Amsterdam, the Netherlands

[3]Corresponding author: Nynke H. Dekker
E-mail: N.H.Dekker@tudelft.nl
Phone: +31-152783219

Supplementary Information

Tables S1-S7

Figures S1-S7

SUPPLEMENTARY MATERIALS AND METHODS

Double-stranded RNA constructs for magnetic tweezers experiments
Overview of the protocol. Here we give an overview of the protocol to generate the dsRNA magnetic tweezers construct. In brief, our protocol to generate fully double-stranded RNA constructs is based on annealing two complementary single-stranded RNA molecules that carry multiple biotin or digoxigenin labels at their respective 5' ends (**Fig. 1c**). The product of the annealing reaction is a 4218 bp fully double-stranded RNA construct with multiple biotin labels at one end and multiple digoxigenin labels at the other end that enable attachment to streptavidin-coated magnetic beads and the anti-dig-coated flow surface, respectively (**Fig. 1e**). Prior to the final annealing step, the two single-stranded RNA molecules are prepared in separate reactions by T7 *in vitro* transcription from DNA templates (**Fig. 1c,d**). The T7 transcription proceeds in two steps. In an initial step, short sequences that contain only three of the four nucleotides are transcribed in the presence of biotin- or digoxigenin-labeled nucleotides and the polymerase is stalled at the fourth nucleotide that is omitted from the reaction mixture. The stalled polymerase complexes are purified and transcription is reinitiated in the presence of all four unlabeled nucleotides to complete the single-stranded RNA molecules (**Fig. 1c**).

Construction of the DNA templates. The DNA templates for RNA transcription are generated by PCR from a pBAD plasmid using hotstart Herculase (Agilent) with nucleotide concentrations of 200 nM (Promega) and appropriately chosen primers (see below). The final DNA template for the biotin-labeled (digoxigenin-labeled) strands consists of a T7 promoter followed by a 33 nt sequence that contains 12 A, but no T (12 T, but no A), in turn followed by a 4.2 kb sequence starting in T (starting in A). The resulting PCR products are column purified using the Nucleospin Gel and PCR purification kit (Macherey Nagel) according to the vendor's protocol, and imaged by gel electrophoresis.

Forward primer biotin-labeled strand:
5'-TAATACGACTCACTATAGGGAGACCAGGACCAGACCAGGACCAGACCAG
GACC**TAAGATTAGCGGATCCTACCTGAC** 3'
Reverse primer biotin-labeled strand:
5'-GGGTGTCCTGGTCCTGTCCTGGTCCTGTCCTGGTCCAGGTTAACCTCAA
CTTCCATTTCC 3'

Forward primer digoxigenin-labeled strand:
5'-TAATACGACTCACTATAGGGTGTCCTGGTCCTGTCCTGGTCCTGTCCTGG
TCC**AGGTTAACCTCAACTTCCATTTCC** 3'
Reverse primer digoxygenin-labeled strand:
5'-GGGAGACCAGGACCAGACCAGGACCAGACCAGGACCTAAGATTAGCGG
ATCCTACCTGAC 3'

Two-step T7 in vitro *transcription.* The purified PCR products are used as templates in T7 *in vitro* transcription reactions. Initial transcription reactions are carried out using the

Ribomax Large Scale RNA production kit-T7 (Promega) with a reaction mix containing 16 nM GTP, CTP, and biotinylated-ATP (Perkin Elmer), but no UTP (16 nM GTP, CTP, digoxigenated-UTP, but no ATP) and a 10-fold reduced T7 polymerase concentration (compared to the vendor's protocol) for 10 min at room temperature. During the initial transcription reactions, 12 biotin labels (12 digoxigenin labels) are incorporated and the polymerase subsequently stalls at the missing fourth nucleotide. The stalled polymerase complexes are purified twice on Illustra Microspin G25 size exclusion columns according to the vendor's protocol. To block free polymerases, we subsequently add 25 µg/µl heparin (heparin sodium salt from porcine intestinal mucosa; Sigma) to the reactions and incubate for 5 min at room temperature. To complete the 4.2 kb single-stranded RNA molecules, we reinitiate the transcription reactions in the presence of 1.5 mM of all four unlabeled NTPs in the reaction mixture and incubate for 1 h at room temperature. After completion of the transcription reactions, we add DNase (1 unit/µg of template DNA), incubating for 20 min at 37 °C to fully digest the DNA templates. Subsequently, we purify the single-stranded RNA molecules on RNeasy columns according to vendor's protocol (Qiagen). The resulting RNA concentrations are determined using a Nanodrop photospectrometer (Isogen Life Sciences). Once the single-stranded RNA molecules are complete, we anneal them in equimolar amounts (typically between 500-1000 ng) in a buffer containing 75 mM NaCl and 7.5 mM sodium citrate, with a final volume of 100 µl. Hybridization is performed in an Eppendorf thermocycler (Mastercycler Personal) by incubating for 60 min at 65 °C, and subsequently cooling down in steps of 1.2 °C and 1.3 °C alternating every 5 min to a final temperature of 25 °C to yield to the final double-stranded product. The resulting double-stranded RNA product is purified on a RNeasy column, eluted in 1xTE buffer containing 1% ethanol, and stored at -80 °C prior to use in the magnetic tweezers.

Magnetic tweezers for single-molecule measurements
Buffers for magnetic tweezers measurements. Measurements were performed in TE buffer (Sigma), pH 8.0, containing 10 mM Tris-HCl and 1 mM EDTA (ethylenediaminetetraacetic acid), supplemented with SUPERase·In RNase inhibitor (Ambion) at a final concentration of 0.1 unit/µl and with varying amounts of NaCl added, unless otherwise noted.

Double-stranded DNA constructs with PCR-generated "handles" for magnetic tweezers measurements. For reference measurements on dsDNA in the MT, we employed either 3.4 kbp or 20.6 kbp dsDNA constructs with multiple biotin and digoxigenin labels at their respective ends. Biotin or digoxigenin labeled dsDNA was generated in PCR reactions that included labeled nucleotides and the labeled PCR products were attached to the central, unlabeled dsDNA molecule by ligation, as described previously (1). The 20.6 kbp dsDNA molecule (45.6% GC content) is based on the Supercos1-lambda1,2 plasmid and was used previously (2, 3); details of the protocol are given in Ref. (1). The 3.4 kbp dsDNA (45.8% GC content) was selected to match the contour length of dsRNA and is based on the pRL-SV40 plasmid (Promega) digested with BamHI and XbaI and again ligated to PCR-generated DNA handles containing biotin or digoxigenin, respectively.

Double-stranded DNA constructs with labels on only one strand at each end. For control measurements, we created a dsDNA construct that has biotin and digoxigenin labels for bead and surface attachment, respectively, on only one strand at each end, similar to our dsRNA construct and unlike the PCR-generated standard dsDNA constructs for MT measurements (described in the previous section). Single-strand labelling of dsDNA was achieved by single-strand nicking followed by a Klenow fill-in reaction. We started with the pRL-SV40 plasmid DNA (Promega Corporation, Madison, WI). To introduce restriction sites for the nicking enzymes Nt-*Bbv*CI and Nb-*Bsm*I and the restriction enzyme *Sma*I, forward oligo 5'-P GATCCCTCAGCGGGAGACCAGGACCAGACCAGGACCAGACCAGGACCCGGG ACCAGGACAGGACCAGGACAGGACCAGGACACCCGAATGCG was annealed to reversed oligo 5'-P- CTAGCGCATTCGGGTGTCCTGGTCCTGTCCTGGTCCTGTCCTGGTCCCGGGTC CTGGTCTGGTCCTGGTCTGGTCCTGGTCTCCCGCTGAGG and ligated into *Bam*HI- and *Xba*I-digested pRL-SV40. The resulting plasmid pRL-SV40-BbvCI-BsmI was amplified and subsequently linearized with *Sma*I and the top strand nicked with Nt-*Bbv*CI (New England Biolabs, Ipswich, MA). The 5' 42bp-fragment was melted out and filled in with Klenow using a mixture of nucleotides containing dTTP, dCTP, dGTP (purchased from Promega Corporation, Madison, WI) and Bio-14-dATP (Invitrogen/Life Technologies). After purification, the bottom strand of pRL-SV40-BbvCI-BsmI was nicked with the nicking enzyme Nb-*Bsm*I (New England Biolabs, Ipswich, MA). The 42bp-fragment was melted out and filled-in with Klenow using a mixture of nucleotides containing dATP, dCTP, dGTP (purchased from Promega Corporation, Madison, WI) and Dig-11-dUTP (Roche Applied Science). Remaining nicks were closed by T4 DNA ligase.

Magnetic tweezers set up. Our MT implementation has been described previously (1, 2, 4, 5). Briefly, a 100× oil-immersion objective (Olympus ACH 100X; numerical aperture (NA) = 1.25) connected to a CCD camera (Pulnix TM-6710CL) was used to image superparamagnetic beads tethered by dsRNA molecules to the surface of a flow cell. Flow cells were made from glass microscope cover slips with a double layer of parafilm as a spacer. The bottom surface was coated with nitrocellulose (0.1% (wt/vol) in amyl acetate) and flow cells were stored dry. Before measurements, flow cells were extensively rinsed with RNaseZap (Invitrogen), followed by rinsing with milliQ water, and rinsing with TE + 200 mM NaCl buffer. 3.0-µm-diameter nonmagnetic latex beads (Invitrogen) were aspecifically attached to the bottom surface by incubation in TE + 200 mM NaCl buffer for 30 min to act as reference beads. Before addition of the RNA construct to the flow cell, the bottom surface was functionalized by incubation with 100 µg·ml⁻¹ anti-digoxigenin (Roche) in PBS buffer (Sigma) for 60 min to provide for RNA attachment and was passivated by incubating for 30 min with 2 mg·ml⁻¹ bovine serum albumin (Sigma) in TE + 200 mM NaCl buffer. The functionalized RNA constructs were incubated in the flow cell for 30 min at a final concentration of ~0.1 ng/µl in TE + 200 mM NaCl buffer. Streptavidin-coated superparamagnetic MyOne beads (Invitrogen) or M270 beads (Invitrogen) were diluted 50-fold in TE + 200 mM NaCl buffer, flushed into the flow cell, and incubated for 30 min. Finally, unattached beads were flushed out with TE + 200 mM NaCl buffer.

The positions of a dsRNA-tethered bead and a reference bead attached to the surface were tracked simultaneously at a rate of 120 Hz. From analysis of the CCD images, the bead positions in *x*, *y* and *z* were determined (6, 7). After subtraction of the reference bead position to correct for mechanical drift, the tethered bead was tracked with an accuracy of ~1-2 nm in the *x*, *y* and *z* dimensions.

Force calibration in the magnetic tweezers. We determined the stretching force applied in the MT (i.e. the magnetic force pulling the bead away from the surface) from analysis of the bead's fluctuations, using the relationship (8):

$$F = L \cdot k_B T / \mathrm{Var}(x) \quad (1)$$

where *L* is the tether extension, determined as the mean of the *z*-position above the surface, k_B is Boltzmann's constant, *T* the absolute temperature and $\mathrm{Var}(x)$ is the variance of the fluctuations in the *x* (i.e. in-plane) position. In order to determine $\mathrm{Var}(x)$ accurately, biases due to the finite acquisition speed of the CCD camera need to be taken into account (7, 9-11). We utilized the method that determines the force from the integrated power spectral density of the *x*-fluctuations using iteratively applied corrections for the finite camera acquisition frequency (10). Control calculations, using a method that analyzes the power spectral density using a closed-form expression to account for corrections and a method that analyzes the fluctuations in real space using the Allan variance (11) gave identical results, within experimental error (**Fig. S1a**). For the rotation-extension measurements (**Figs. 2, 4,** and **5**) and for dynamic force spectroscopy measurements (12) (**Fig. S2c,d**), we used the forces from pre-determined relationships of magnetic position and applied stretching force for our experimental configuration (**Fig. S1b,c**).

Magnetic tweezers for torque measurements. The magnetic torque tweezers (MTT) are a variant of the magnetic tweezers in which the pair of rectangular magnets (**Fig. 1d**) is replaced by cylindrical permanent magnet to apply forces and a smaller side magnet to apply torques (13) (**Fig. 3a** and **Fig. S4a**). Alternatively, two pairs of Helmholtz coils arranged in (*x,y*)-plane can be used to apply torques, an approach termed electromagnetic torque tweezers (eMTT) that allows one to set the torsional stiffness of the angular trap independently of the magnitude of the applied stretching force (14) (**Fig. S4b**). The torque measurement relies on tracking the rotation angle *θ* of the bead about the *z*-axis, i.e. the nucleic acid tether axis (13). The torsional trap stiffness k_θ was calibrated for each measurement from the variance of the rotational fluctuations $\mathrm{Var}(\theta)$:

$$k_\theta = k_B T / \mathrm{Var}(\theta) \quad (2)$$

If a torsionally constrained nucleic acid tether is over- or underwound away from its torsionally relaxed equilibrium angular position (θ_0), the resulting restoring torque leads to a shift in the mean of the angular fluctuations $\Delta\theta = \langle \theta_N - \theta_0 \rangle$, where θ_N is the angle position after *N* turns and $\langle \ldots \rangle$ denotes the mean (13). The restoring torque exerted by the nucleic acid tether was calculated as:

$\Gamma = - k_a \cdot \Delta\theta$ (3)

The rotation angle can be monitored either directly through the use of an angular marker and image analysis (13, 15) or indirectly by converting the (*x,y*)-position of the bead to angular and radial coordinates (14, 16) (**Fig. S4c,d**). Torque measurements were carried out both using the MTT set up described by Lipfert *et al.* (13) and the eMTT instrument described by Janssen *et al.* (14). In both cases, we employed the angle tracking protocol based on conversion from (*x,y*)-position and custom-made cylindrical magnets consisting of a stack of 6 magnets each 1 mm in height (for 6 mm total height), 6 mm in diameter and with a central aperture of 1 mm in diameter. For some measurements, a cylindrical magnet was used in which the last magnet in the stack was assembled with opposite magnetization direction; this "flipped" magnet assembly has been shown to give larger forces than a similar magnet stack where all magnets have the same magnetization direction (17). Forces in the MTT and eMTT were calibrated as described in the "Force calibration in the magnetic tweezers" section, except that the variance of the radial component of the fluctuations was used instead of the *x*-position (16).

Elastic rod model for dsDNA and dsDNA
Isotropic rod model of polymer elasticity. The elasticity of twist-storing biopolymers can be modeled in the framework of the isotropic rod model (18). The isotropic rod model has been, in particular, used as a coarse grained model for dsDNA that neglects specific sequences effects and is expected to be valid on length scales much longer than one base pair. The deformations of a segment of an isotropic rod (**Fig. 1b**) can be described by three quantities: 1) the stretch or extensional deformation *u*(*s*) that measures the fractional change in the length of the segment, 2) the bend or bending deformation *β*(*s*) that measures how the tangent vector *t*(*s*) changes along the rod, and 3) the twist density or torsional deformation *ω*(*s*) that determines how the each segment is rotated around the axis of the rod with respect to adjacent segments, where *s* is denotes the coordinate along the rod. The total elastic energy of the rod is given by integrating contributions *dE*(*s*) along its total length (18):

$E = \int dE(s)ds = k_B T/2 \int_0^{\text{Ltot}} (A\beta^2 + Bu^2 + C\omega^2 + 2Du\omega)ds$ (4)

where the respective terms in the rightmost integral in turn represent contributions from bending energy, stretching energy, twisting energy, and twist-stretch coupling energy. Note that the upper limit of the integrand equals L_{tot}, the total length of the stretched rod, which may exceed the contour length L_C. Each term comes with a phenomenological coupling constant: *A* is the bending persistence length (in units of length), *B* is the stretch modulus (in units of inverse length), which is more commonly expressed as $S = B \cdot k_B T$ (where *S* is the stretch stiffness in units of force), *C* is the torsional persistence length (in units of length), and *D* is the (dimensionless) twist-stretch coupling.

Inextensible and extensible WLC models. A further simplification of **Eq. 4** is the inextensible worm-like chain (WLC) model that assumes the polymer to be torsionally unconstrained and inextensible (19-21). The elastic energy in the inextensible WLC

6

model simplifies to the first term, i.e. the bending energy term, in the integral in **Eq. 4**. The inextensible WLC model provides an accurate description of the stretching behavior of dsDNA (19-21) and dsRNA (22, 23) in the absence of torsional strain and for low forces, i.e. in the limit that $F \ll B \cdot k_B T$, the so-called enthalpic stretching regime. The WLC model has been solved numerical to yield the force F as a function of the molecule's extension z and a number of approximation formulae exist. In this work, we use the seventh order approximation to the numerical solution due to Bouchiat et al. (24):

$$F(z) = k_B T/A \cdot [1/4(1-z/L_C)^2 - \tfrac{1}{4} + z/L_C + \Sigma_{i=2,...,7} \, \alpha_i \, (z/L_C)^i \,] \qquad (5)$$

in which the contour L_c and the bending persistence length A are treated as free parameters. The α_i are numerical coefficients given in Ref. (24). For higher forces, $F > 5$-10 pN for dsDNA and dsRNA, elastic stretching contributions become relevant and the force-extension data can be described using the extensible WLC model (24-27). In the extensible WLC model, the terms z/L_C in **Eq. 5** is replaced by $z/L_C - F/S$ (Ref. (24)).

Models of dsDNA and dsRNA under torsional constraint. Fully double-stranded DNA or RNA molecules that are free of nicks and attached via multiple attachment points at both ends can experience torsional strains, giving rise to a complex force-torque response. A useful quantity to describe twist-storing polymers under torsional constraint (6, 28) is the linking number Lk. The linking number is a topological invariant for torsionally constrained molecules (29-31) and partitions into twist Tw and writhe Wr:

$$Lk = Tw + Wr \qquad (6)$$

Essentially, Tw is the number of turns in the double helix and Wr is the number of times the helical axis crosses itself. Magnetic tweezers and magnetic torque tweezers control Lk of the molecule under study. It is convenient to consider the linking number with respect to the torsionally relaxed molecule: this is the definition for the number of applied turns used throughout the text (**Figs. 2-5** and **Fig. S3**), i.e. zero turns corresponds to a torsionally relaxed molecule. For a torsionally relaxed molecules $Lk_0 = Wr_0 + Tw_0$ with $Wr_0 = 0$ and Tw_0 being equal to the natural twist of the double helix, i.e. the number of base pairs divided by ~10.5 base per turn for dsDNA and ~11.3 base pairs per turn for dsRNA (32). Another useful quantity in this context is the supercoiling density, defined as $\sigma = (Lk - Lk_0)/Lk_0$, which is normalized to the natural twist of the molecule (**Figs. 2-4** and **Fig. S3k,l**).

For small deviations of the linking number away from the torsionally relaxed equilibrium state, the change in linking number is initially absorbed by elastic twist deformations for both dsDNA (8, 13, 15, 33, 34) and dsRNA (**Fig. 3**). In this regime, the torque increases linearly with the number of applied turns N:

$$\Gamma = 2\pi \cdot N \cdot k_B T \cdot C / L_C \qquad (7)$$

While it is possible to include non-linear terms into the twist response close to zero applied turns, the current data are well-described by a linear model (13, 33, 35) (**Fig. 3c**).

C in **Eqn. 7** is the effective twist persistence length, since bending fluctuations decrease the effective twist persistence compared to its intrinsic value (36, 37). Moroz and Nelson have developed a model of the force-dependence of the effective torsional stiffness (36, 37). They use a perturbative approach, valid in the high-force limit; to third order in $F^{-1/2}$, their model gives (16, 38):

$$C = C_{\lim}\left(1 - \frac{C_{\lim}/A}{4\left(\frac{AF}{k_BT}\right)^{1/2}} + \frac{\left(C_{\lim}/A\right)^2 - 2\left(C_{\lim}/A\right)}{16\left(\frac{AF}{k_BT}\right)} - \frac{4\left(C_{\lim}/A\right)^3 - 16\left(C_{\lim}/A\right)^2 + 21\left(C_{\lim}/A\right)}{256\left(\frac{AF}{k_BT}\right)^{3/2}}\right) \quad (8)$$

where $C_{\lim}$ is the intrinsic twist persistence length, adopted in the high-force limit. While **Eqn. 8** provides a reasonable qualitative description of the data, we observe deviations from the model at low forces (< 2 pN) for both dsDNA (13, 16) and dsRNA (**Fig. 3f**), likely, at least in part, due to the high-force perturbative approach of the model. We obtain $C_{\lim}$ from fits of **Eqn. 8** to the $C(F)$ data at forces > 2.5 pN; this cut-off is an empirical choice, giving values for $C_{\lim}$ of dsDNA consistent with previous extrapolations to high stretching forces as well as with direct measurements at high forces (13, 33).

DsRNA or dsDNA molecules that are twisted further away from their torsionally relaxed equilibrium conformation beyond the linear torque response regime, undergo conformational changes, giving rise to a complex force-torque phase diagram (**Fig. 3g**). While a number of models have been proposed to describe aspects of this force-torque diagram for dsDNA (see e.g. (39-49)), there is currently no commonly accepted model that quantitatively accounts for all aspects of the diagram. Here, we limit the discussion to relatively simple models that account for the formation of plectonemic supercoils as the linking number is increased beyond the critical supercoiling density for buckling.

A basic model of plectonemic supercoiling considers the twist energy and the energy required to form a circular loop (6, 28). This simple model makes predictions for the buckling torque Γ_{buck}, the slope of the extension vs. turns response in the plectonemic regime $\Delta L/$turn, and for the number of turns at which buckling occurs N_{buck}:

$$\Gamma_{\mathrm{buck}} = (2A \cdot k_BT \cdot F)^{1/2} \qquad (9)$$

$$\Delta L/\mathrm{turn} = \pi \cdot (2A \cdot k_BT / F)^{1/2} \qquad (10)$$

$$N_{\mathrm{buck}} \approx L_C \cdot (A \cdot F / (2\pi^2 \cdot C^2 \cdot k_BT))^{1/2} \qquad (11)$$

We note that these model predictions do not have any free parameters, since A, L_C, and C can be determined independently from force-extension measurements (**Fig. S2** and **Fig. S1d-f**), and torque-turn measurements (**Fig. 3c**), respectively. The simple model gives the right trends but only qualitative agreement with our measurements for Γ_{buck}, $\Delta L/$turn, and N_{buck} (dashed lines in **Fig. 2b,c** and **Fig. 3e**). Quantitative deviations are to be expected,

given the many approximations inherent in the model, including the neglect of thermal fluctuations and the consideration of a circular loop only.

A more refined model is due to Marko (50), which includes an additional parameter, the torsional stiffness of the plectonemic state P. The expressions for the buckling torque Γ_{buck}, the slope of the extension vs. turns response in the plectonemic regime $\Delta L/\text{turn}$, and for the critical supercoiling density σ_{buck} in the Marko model (following the notation of Wang and coworkers (34)) are:

$$\Gamma_{\text{buck}} = (2 \cdot k_B T \cdot P \cdot g \,/\, (1\text{-}P/C))^{1/2} \tag{12}$$

$$\Delta L/\text{turn} = \cfrac{\dfrac{2\pi}{\omega_0}\left[1 - \dfrac{1}{2}\sqrt{\dfrac{k_B T}{Af}} - \dfrac{\omega_0^2 C^2}{16}\left(\dfrac{k_B T}{Af}\right)^{3/2}\left(\dfrac{1}{c}\sqrt{\dfrac{2pg}{1-p/c}}\right)^2\right]}{\sqrt{\dfrac{2pg}{1-p/c}}\left(\dfrac{1}{p}-\dfrac{1}{c}\right)} \tag{13}$$

$$\sigma_{\text{buck}} = 1/c \cdot (2 \cdot p \cdot g \,/\, (1\text{-}P/C))^{1/2} \tag{14}$$

with $g = F - (F \cdot k_B T / A)^{1/2}$, C is the torsional twist stiffness, approximated by the model of Moroz and Nelson, and $p = k_B T \cdot P \cdot \omega_0^2$ and $c = k_B T \cdot C \cdot \omega_0^2$ are scaled quantities related to P and C (where ω_0 is 2π divided by the helical pitch). We fit the value of P independently to the critical supercoiling density data (**Fig. 2b**), to the slopes in the plectonemic regime (**Fig. 2c**), and to the critical torque data for buckling (**Fig. 3e**) for dsRNA and obtain consistent results, within experimental error, with $P_{\text{RNA}} \sim 22$ nm. We use the model by Brutzer *et al.* (51) that essentially extends the treatment due to Marko (50) to analyze the buckling transition (see the "Two-state model of the buckling transition" section).

Determination of the twist-stretch coupling from the slope of rotation-extension curves. The twist-stretch coupling parameter D can be determined from the change in extension upon over- and underwinding the molecule (52-54). At forces sufficiently large to suppress strong bending fluctuations, the energy per length of a stretched and twisted dsRNA or dsDNA molecule can be expressed by modifying **Eqn. 4** and adding a term $-F \cdot u$ to account for the energy contribution of the external force:

$$E/L = k_B T/2 \cdot (A\beta^2 + Bu^2 + C\omega^2 + 2Du\omega) - F \cdot u \tag{15}$$

Minimize the energy with respect to u at constant ω and F, we find

$$k_B T/2 \cdot (2Bu + 2D\omega) - F = 0 \tag{16}$$

Considering now two measurements at the same force, one at an arbitrary value of the twist ω and a second for a torsionally relaxed molecule $\omega = 0$, we subtract the expressions and obtain:

$$B(u - u_{\omega=0}) + D\omega = 0 \tag{17}$$

The slope of the rotation extension curve is then given by

$$d(u - u_{\omega=0})/d\omega = -D/B \tag{18}$$

Alternatively, expressing the slope as the change in length ΔL per applied turns, we can write

$$d\Delta L/dN = -2\pi D/B \tag{19}$$

This then gives an expression for D equal to:

$$D = -(d\Delta L/dN)\cdot B / (2\pi) = -(d\Delta L/dN)\cdot S / (2\pi\cdot k_B T) \tag{20}$$

The uncertainty $\Delta(D)$ in D is given by standard propagation of errors:

$$\Delta(D)/D = ([\Delta(d\Delta L/dN) / (d\Delta L/dN)]^2 + [\Delta(S)/S]^2)^{1/2} \tag{21}$$

We note that instead of the dimensionless twist-stretch coupling parameter D that we use in this work, some authors employ $g = k_B T\cdot D$ (with units of energy; see, e.g., Ref. (53)) or $D' = D/(1.85/nm)$ (with units of length; see, e.g., Ref. (52, 54)). Here, we consistently employ the dimensionless convention for D.

Models for the twist-stretch coupling and experimental results for dsDNA. Naïve intuition suggests that a helical rod shortens as it overwound, or, equivalently, unwinds as it is stretched. Early work based on interpretation of single-molecule stretching and twisting experiments suggested that dsDNA indeed shortens upon overwinding, i.e. that it exhibits a positive twist-stretch coupling D (Refs. (52, 55)). Marko (55) analyzed the DNA overstretching data of Cluzel *et al.* (56) in the framework of an elastic model with a stable overstretched state and found a value of $D_{DNA} = 30$. Kamien *et al. (52)* analyzed the DNA length response upon overwinding in the magnetic tweezers data of Strick *et al.* (8) and determined $D_{DNA} = 22$, similarly with a positive sign. The apparent positive twist-stretch coupling was explained in terms of simple elastic models that described dsDNA as an isotropic material with a helical shape (52, 55). Similarly, a higher resolution model with coarse−grained representations for each base found a positive D for dsDNA (57). In addition, atomistic molecular dynamics simulations also found positive values for the twist-stretch coupling, in the range of $D_{DNA} = 7.5 - 33$ (Ref. (58)).
However, the initial estimates of D from experimental data included regions where the dsDNA underwent structural transitions, such as melting and overstretching, and were not representative of the behavior of dsDNA close to its unperturbed B-form structure. Higher resolution MT experiments found that dsDNA lengthens upon overwinding, indicative of a negative D value (53, 54). Lionnet *et al. (54)* found a slope of 0.42 ± 0.2 nm/turn, independent of salt concentration and stretching force up to ~15 pN, and deduced $D_{DNA} = -16 \pm 7$. Gore *et al. (53)* obtained a similar value for the length increase upon overwinding of 0.5 ± 0.1 nm/turn, corresponding to $D_{DNA} = -22 \pm 5$. In addition,

Gore *et al.* employed a rotor bead assay to directly monitor the change in equilibrium twist upon stretching of DNA and found that stretching by 1% leads to an increase in twist by ~0.1%, in agreement with the value for the twist-stretch coupling obtained from the magnetic tweezers measurements (53). Using the rotor bead assay, they found that for large stretching forces (> 30 pN) the twist-stretch coupling changes sign and becomes positive. Recently, Sheinin and Wang (59) employed an optical torque wrench assay to simultaneously monitor the extension and torque upon overwinding DNA. They analyzed their data in the framework of a model that goes beyond the linear extension response to winding and includes the effect of bending fluctuations, allowing a fit of the data over a larger range of σ values. They found D_{DNA} = -21 ± 1, independent of force up to ~10 pN (Ref. (59)), consistent with the earlier measurements by Gore *et al.* and Lionnet *et al*. In this work, we limited our analysis of the rotation response to the range -0.01 < σ < 0.02 and found that approximating the DNA response as linear only leads to small corrections compared to the full non-linear model.

A negative twist-stretch coupling can be rationalized by models that include a stiff helical backbone wrapped around a softer core material (53, 60). In addition, several higher resolution models with atomistic representation of dsDNA were consistent with negative values for the twist-stretch coupling (54, 61, 62).

Models for the twist-stretch coupling of RNA. Experimentally, we found a positive twist-stretch coupling for dsRNA, based on the observation that dsRNA shortens by 0.85 ± 0.04 nm per turn upon overwinding. We note that including the non-linear terms as described by Wang and coworkers (59) did not significantly affect our results. How can this surprising result be understood in terms of molecular models? The observed positive twist-stretch coupling for dsRNA could be rationalized in terms of the simple elastic models of a helical isotropic material initially proposed for dsDNA (52, 55). In essence, a helix with a constant radius must shorten as it is overwound (53, 54). However, this approach is unsatisfying since it evidently fails for dsDNA.

The experimental observation of a negative twist-stretch coupling for dsDNA led to the proposal of models that feature a stiff backbone wrapped around an isotropic core (53, 60) and involve a change in helix radius upon overwinding. These stiff backbone models correctly account for the negative twist-stretch coupling for dsDNA. However, they predict the twist-stretch coupling of dsRNA to also be negative. For example, the "toy model" by Gore *et al. (53)* predicts an even more pronounced negative twist-stretch coupling for dsRNA compared to dsDNA due to its smaller helix angle, in clear contrast to our experimental results.

The apparent failure of simple elastic models to satisfactorily account for the twist-stretch coupling of both dsDNA and dsRNA in a unified framework might suggest that at least some of the microscopic details of the molecules need to be taken into account for quantitative predictions of *D*. Kosikov et al. simulated dsDNA poly-AT and poly-GC homopolymers, employing all-atom potentials for the nucleic acid and an implicit treatment of the solvent and ion atmosphere in a molecular mechanics framework (63). These authors found, for conformations close to the equilibrium values for the helical rise, that A-form dsDNA untwists upon stretching and B-form dsDNA overtwist upon stretching, in qualitative agreement with our results for dsRNA and dsDNA. Quantitatively, their constant stretch, variable twist simulations predict slopes of ~ −3°

per 0.1 nm stretching for A-form dsDNA and ~ +3° per 0.1 nm stretching for B-form dsDNA (where the exact values depend on the fitting range and conformational family considered). In order to determine the value of the twist-stretch coupling D from these slopes that were obtained in the imposed stretch, variable twist ensemble, one needs to consider an argument similar to the derivation outlined in Eqns. 15-20. However, in contrast to the imposed twist, variable stretch ensemble considered in Eqns. 15-20, the minimization is with respect to the twist ω, at constant u. The result analogous to Eqn. 18 in the imposed stretch, variable twist ensemble is $D = -C \cdot (\Delta\omega/\Delta u)$. Consequently, the prediction from the slopes are $D_{DNA} \sim -50$ and $D_{RNA} \sim +50$. These predictions have the correct sign but are in absolute value too large by a factor of 3-5 in magnitude, compared to the experimental results.

We have modeled dsRNA and dsDNA using the framework of six base-step parameters (see the "Base-step parameter model" section), which presents an intermediate resolution model. Ultimately, a full understanding of the striking differences in the twist-stretch behavior might require modeling with a full atomistic descriptions of the nucleic acids, ions, and solvent and presents an interesting challenge for molecular dynamics simulations or related approaches.

Two-state model of the buckling transition. We use the two-state model by Brutzer *et al.* *(51)* to analysis the tether extension data at the buckling transition and to determine the characteristic timescale for buckling τ_{buck} (**Fig. 5**). Briefly, prior to buckling after N applied turns the free energy of the DNA is given by

$$E_{pre}(N) = 0.5 \cdot C/L_C \cdot (2\pi)^2 \cdot N^2 \tag{22}$$

The free energy after buckling is equal to

$$E_{post}(N) = E_b + 0.5 \cdot C/L_C \cdot (2\pi)^2 \cdot (N - \Delta N_b)^2 \tag{23}$$

where E_b is the energetic penalty that must be overcome for the formation of the buckling structure and ΔN_b is the amount of twist (in number of turns) that is transferred into writhe during buckling. The probability that the post-buckling state is occupied p_{post} is given in the framework of this simple two-state model by Boltzmann statistics:

$$p_{post} = 1/(1+\exp[(E_{post} - E_{pre})/k_BT]) \tag{24}$$

Inserting the expression for E_{pre} and E_{post} the probability can be written as:

$$p_{post} = 1/(1+\exp[(C/L_C \cdot (2\pi)^2 \cdot (N_b - N) \cdot \Delta N_b)/k_BT]) \tag{25}$$

where N_b equals the number of applied turns at the point of buckling equilibrium, i.e. the number of turns where $E_{pre} = E_{post}$. By fitting the dependence of the post-buckling population on the number of applied turns to this expression for the probability, we determined both N_b and ΔN_b (**Fig. 5c** and **Fig. S5l**). Notably, we find that the fitted values for ΔN_b for our 4.2 kbp dsRNA tethers are consistently larger than one, i.e. that more than one full turn is converted from twist to writhe at the buckling transition, similar to what is

observed for dsDNA (Ref. (51) and **Fig. S5l**). In addition, we find ΔN_b for dsRNA to increase weakly with increasing force and salt concentration, again qualitatively similar to what has been observed for dsDNA (51).

To describe the dependence of the mean residence times in the pre- and post-buckling states, τ_{pre} and τ_{post}, on the number of applied turns in the two-state framework, we assume an Arrhenius relationship with an exponential dependence on the number of applied turns (51). The expression for the mean residence time of the pre-buckling state is

$$\tau_{\text{pre}} = \tau_{\text{buck}} \cdot \exp[-(C/L_C \cdot (2\pi)^2 \cdot (N_b - N) \cdot \Delta N_{\text{pre}})/k_B T] \qquad (26)$$

where τ_{buck} is the overall characteristic residence time at the buckling transition and ΔN_{pre} is the angular distance to the transition state from the pre-buckling state. A similar expression holds for τ_{post}, only with ΔN_{pre} replaced by $-\Delta N_{\text{post}}$, the angular distance to the transition state from the post-buckling state. Fits of the simple exponential, Arrhenius-like dependence to the pre- and post-buckling residence times (**Fig. 5c**) were used to determine the overall characteristic residence time τ_{buck} as a function of applied force and salt concentration (**Fig. 5e**).

The estimates of τ_{pre}, τ_{post}, and consequently τ_{buck} are possibly biased due to the limited time resolution of our instrument and due to the need to filter the data prior to applying a threshold (**Fig. S5a-d**). To estimate the effects of the finite sampling frequency, we analyzed the data using sliding average filters of different width in the range of 40 to 10 Hz. For the dsRNA buckling data, using the filters of different width did not affect the results for τ_{buck}, within experimental error. In addition, we tested the effect of correcting τ_{pre} and τ_{post} for the finite acquisition time by applying a statistical correction method based on the moment equations for a two-state Markov model (64). In brief, given observed values τ_{pre} and τ_{post} measured with a detection limit of time ξ (which is set by the camera frequency and width of the filter), the corrected "true" values τ^*_{pre} and τ^*_{post} are determined by (numerically) solving the two equations (64):

$$\tau_{\text{pre}} = (\tau^*_{\text{pre}} + \tau^*_{\text{post}}) \cdot \exp(\xi / \tau^*_{\text{post}}) - \tau^*_{\text{post}} \qquad (27)$$

$$\tau_{\text{post}} = (\tau^*_{\text{pre}} + \tau^*_{\text{post}}) \cdot \exp(\xi / \tau^*_{\text{pre}}) - \tau^*_{\text{pre}} \qquad (28)$$

While fitting the corrected values for τ_{pre} and τ_{post} (**Eqn. 27** and **28**) gave slightly lower buckling times τ_{buck}, compared to fitting the uncorrected data, the results were within experimental error and differed at most by a factor of two for the fastest dsRNA buckling times (**Fig. S5h**). In contrast, the dwell times in the pre- and post-buckling states are much smaller for dsDNA, compared to dsRNA (**Fig. 5d**). For the dsDNA data, changing filter settings and applying the corrections for the finite detection limit both tended to significantly affect the resulting values for τ_{buck}. Therefore, we only report an upper limit for the characteristic buckling for dsDNA at high force and high salt ($F = 4$ pN and 320 mM monovalent salt; dashed line in **Fig. 5e**). This upper limit of 50 ms is consistent with

the buckling times obtained previously for dsDNA molecules of different lengths (51) (**Fig. 5e**, blue triangles)

Base-step parameter model
As a step beyond the simple isotropic elastic rod model (**Eqn. 4**), we have built a base-pair level model based on the six base-step parameters (65) slide, shift, rise, twist, roll, and tilt (**Fig. S6a**, insets) for dsRNA and dsDNA. Base-pair level models are intermediate between elastic models that treat dsDNA or dsRNA as continuous rods and full atomistic models. Following the approach of Olson and coworkers (66), we have determined the average values and elastic couplings of the base-step parameters by analyzing their observed values in high-resolution crystal structures of nucleic acids deposited in the protein data bank (http://www.rcsb.org/pdb/) using the program 3DNA (67). To ensure data quality, we have only included structures with a resolution of better or equal to 2.8 Å. In addition, we eliminated strongly deformed structures by excluding parameter values that were further than four standard deviations from the mean. To test the sensitivity of our predictions on the data set used, we ran calculations using only structures that did not contain bound proteins ("2.8_noprot" in Table S2) as well as control calculations using a larger data set that included structures with bound proteins ("2.8_all" in Table S2). Additional tests, calculations, and the numerical implementation of our base-step parameter based modeling will be published elsewhere (F.-C.C., J.L., and R.D., *PLOS Computational Biology*, in press).

Comparison of dsRNA and dsDNA geometry. From the distribution of base-step parameters, several observations can be made (**Fig. S6a**). First, the shift and tilt distributions are similar for dsDNA and dsRNA, with average values near zero. Second, dsRNA base-steps have, on average, a negative slide and positive roll, compared to dsDNA base-steps that have approximately zero slide and roll. Third, both dsRNA and dsDNA have positive values for rise and twist, with dsRNA taking on smaller values for these two parameters, on average, compared to dsDNA.

These parameter differences at the level of base-pair steps correspond to the geometric differences observed between idealized B-form dsDNA and A-form dsRNA (see, e.g., **Fig. 1a**). In particular, the negative slide and positive roll values for dsRNA lead to the axis that connects the base pair centers tracing out a pronounced helix, with a diameter of ~8 Å (**Fig. S5b**). In contrast, the center axis for dsDNA, which has on average close to zero slide and roll, is approximately straight (with a helical diameter of only 0.6 Å; **Fig. S6b**). This helical wrapping or "springiness" of the RNA centerline has several interesting consequences. One implication of this structural difference between dsDNA and dsRNA helices is related to the fact that the base-step parameter rise is not, in general, the same as the "helix length per base pair" often also referred to as (helical) "rise". The average value for the base-step parameter rise is only slightly smaller for dsRNA than for dsDNA (3.22 Å and 3.30 Å, respectively, for the "2.8_noprot" data sets; **Fig. S6a**). In contrast, the helical rise is approximately 20% smaller for dsRNA compared to dsDNA (2.8 Å for dsRNA (22, 23, 68, 69) and 3.3-3.4 Å for dsDNA; see e.g. Ref. (70) and references therein). This difference can be understood from the "springiness" of the RNA centerline; for helices with an (almost) straight centerline, such as dsDNA, the helical rise and the base-step parameter rise are almost identical (and sometimes used

interchangeably). For a "springy" helix, such as dsRNA, the base-step rise does not contribute fully to advancing the helix along its lengths and the helical rise is, therefore, smaller than the base-step rise.

We note that there is a similar distinction between the base-step parameter twist and the overall twist of the helix, i.e. the quantity *Tw* in **Eqn. 6**. This difference was pointed out by Olson and coworkers (71) and taken into account in our calculations. Finally, a comparable distinction has to be made between the twist-rise covariance of the base-step parameters and the overall twist-stretch coupling of the helix (see below).

Simulations of single-molecule experiments based on the base-step parameter model. We carried out simulations based on a Metropolis Monte Carlo sampling scheme that mimic single-molecule stretching and twisting measurements in the MT. For dsDNA, our results are in agreement with previous computational schemes for dsDNA (e.g., through normal mode analysis (72)). Prior modeling of dsRNA is not available, and we chose to carry out direct simulations to ensure rigorous calculation of experimental observables such as global helix linking number, which cannot be computed simply as the sum of base-pair twist, as described above. The calculations are implemented in a software package HelixMC that are being described in detail in a separate publication (Ref. (73); full documentation publically available at http://github.com/fcchou/helixmc). This model makes several simplifying assumptions: i) crystal structures present an accurate sampling of flexibility in solution, ii) the distributions of the six nearest-neighbor base-step parameters give an adequate representation of the molecules, and iii) a purely harmonic elastic treatment is sufficient to capture the fluctuations in solution. Given these assumptions, only approximate agreement with experiments can be expected (74).

From simulated force-extension curves, we determined the bending persistence length and stretch modulus of base-step level model dsDNA and dsRNA molecules (**Table S2**). Similarly, we determined the torsional stiffness and twist-stretch coupling from simulated rotation-torque and rotation-extension curves (**Table S2**). Comparing the results for the "2.8_noprot" and "2.8_all" parameter sets gives a rough estimate of the robustness of our simulation results. In general, the elastic stiffness parameters obtained from the simulations tend to be lower for the "2.8_all" parameter set compared to the "2.8_noprot" parameter set. A possible reason for the slightly lower observed stiffnesses when protein bound structures are included is that the protein bound structures exhibit larger deformations, compared to the protein-less structures, corresponding to larger local flexibility.

The predictions for the bending persistence length are in close to quantitative agreement with the experimental results for both dsDNA and dsRNA (**Table S2**). In addition, simulations with both parameter sets correctly predict A_{RNA} to be ~20% larger than A_{DNA}. The model predictions for the stretch modulus are a factor of ~2 larger than the experimentally measured values for both dsDNA and dsRNA (**Table S2**). Nevertheless, the model correctly predicts S_{RNA} to be ~2-3 fold lower than S_{DNA}. The difference between the stretch modulus between dsDNA and dsRNA originates from the "springiness" of dsRNA. When the helices are stretched, for dsDNA the applied force mostly goes to the increase of rise; but for dsRNA the force can affect both rise and roll, making dsRNA more pliable to global stretching than dsDNA (**Table S3**).

Similarly, while the absolute values of the predicted torsional stiffness C deviate from the experimental results by a factor of ~2, the model correctly predicts them to be of similar size for dsRNA and dsDNA, in particular when considering the "2.8_all" parameter set (**Table S2**). Again, given the assumptions of the modeling, limitations in quantitative agreement were expected.

Nevertheless, we were surprised that predictions of twist-stretch coupling D were in qualitative disagreement with the experiment. While the base-step model predicted the slope in the twist-stretch coupling regime for dsDNA within a factor of two (**Table S2**), it predicts dsRNA to lengthen upon overwinding, in disagreement with our experimental findings.

To produce better working models for dsDNA and dsRNA consistent with our available data, we sought to understand the effect of each parameter in the covariance matrix of the multivariate Gaussian distribution of the six base-step parameters. Due to nonlinearities in relating these microscopic parameters to the elastic rod parameters, understanding these effects required carrying out further simulations after doubling, halving, and reversing the sign of each of the 21 independent parameters in the covariance matrix (**Tables S4 and S5**). These calculations showed that the bending persistence length A is predominantly affected by the variance of tilt and roll, as would be intuitively expected. We also confirmed that the dominant factor controlling torsional persistence length C is the variance of twist. Finally, the twist-stretch coupling of dsDNA is affected by the twist-rise covariance. However, it appears that the twist-stretch coupling D of dsRNA receives substantial contributions form multiple factors, including the covariance of twist-rise, twist-roll, twist-slide, and the variance of twist and roll. This sensitivity of D to multiple microscopic parameters is connected to the "springiness" (displaced helical axis) of dsRNA, such that the effect of stretching is shared by changes in rise, slide and roll and the twist-stretch coupling is acutely sensitive to small changes in the twist-rise, twist-roll and twist-slide covariances. These covariances are themselves small numbers (compared to intrinsic variances of twist, slide, and roll; **Table S6**). This analysis underscores the importance of not conflating measurements of twist-stretch coupling D with the single base-step-level covariance of twist and rise, which have distinct meanings from the experimentally probed global 'twist' and 'stretch', respectively.

Based on the analysis of the effects of the parameters in the covariance matrix (**Tables S4 and S5**), we found that modest modifications of the covariance matrix led to accurate recapitulation of all experimental measured mechanical properties (**Tables S6 and S7**). In particular, the simulations now correctly recovered the positive twist-stretch coupling of dsRNA and gave detailed working models of how both nucleic acid helices responded to force and torque (**Fig. 4d**). These working models are not uniquely defined; the greater number of degrees of freedom in the base pair level covariance model (21) compared to experimental observables (4) necessarily imply that other parameter sets could account for the data as well. Future experimental efforts will be required to pinpoint correct covariance parameters for dsDNA and dsRNA in solution. The current working base-pair level models, which reflect and recover available single-molecule data (**Tables S6** and **S7**; **Figure 4d**), can be integrated efficiently via simulation to give quantitative predictions for observables of other experimental methods such as NMR and X-ray scattering.

TABLES

Table S1: Elastic parameters of dsRNA and dsDNA from single-molecule measurements

Parameter	Symbol (units)	dsRNA, this work	dsRNA, literature	dsDNA, this work	dsDNA, literature
Bending persistence length	A (nm)	57 ± 2	59.4 ± 2.9 Ref. (23) 61 ± 3 Ref. (23)	45 ± 2	47 ± 2 Ref. (75) 43 ± 3 Ref. (34) 44 ± 3 Ref. (13) 47.4 ± 4.4 Ref. (23) 49 ± 2 Ref. (23)
Stretch modulus	S (pN)	350 ± 100	500 ± 29 Ref. (23)	1000 ± 200	1087 ± 94 Ref. (76) 1401 ± 313 Ref. (27) 884 ± 116 Ref. (75) 1266 ± 217 Ref. (75) 935 ± 121 Ref. (23)
Torsional persistence length[†]	C_{lim} (nm)	100 ± 2		109 ± 4	109 Ref. (36) 100 ± 7 Ref. (33) 107 ± 9.8 Ref. (33) 94 ± 7 Ref. (35) 109 ± 4 Ref. (13)
Slope of the extension vs. turns response close to zero turns	$d\Delta L/dN$ (nm/turn)	-0.85 ± 0.04		0.44 ± 0.1	0.42 ± 0.2 Ref. (54) 0.5 ± 0.1 Ref. (53)
Twist-stretch coupling	D (unitless)	11.5 ± 3.3		-17 ± 5	-17 ± 7 Ref. (54) -22 ± 5 Ref. (53) -21 ± 1 Ref. (59)

Measurement in this work are in TE buffer with 100 mM NaCl. The cited literature values were all obtained around physiological pH and in 100-150 mM monovalent salt.
[†]Values for the torsional persistence length are extrapolated to high forces using the Moroz-Nelson model (36, 37) or measured at forces > 15 pN.

Table S2: Predictions of the base-step model for the elastic parameters of dsRNA and dsDNA.

Parameter	Symbol (units)	dsRNA		dsDNA	
		2.8_noprot[1]	2.8_all[1]	2.8_noprot[1]	2.8_all[1]
Bending persistence length	A (nm)	66.3	46.9	54.7	39.4
Stretch modulus	S (pN)	979	776	1956	1504
Torsional persistence length	C_{lim} (nm)	53.0	42.4	28.8	40.5
Slope of the extension vs. turns response close to zero turns	$d\Delta L/dN$ (nm/turn)	0.797	0.650	0.473	0.743
Twist-stretch coupling[2]	D (unitless)	-30.3	-19.6	-35.9	-43.4

[1]The "2.8_noprot" data set contains nucleic acid crystal structures that have been solved to a resolution of better or equal to 2.8 Å and do not include bound proteins; the "2.8_all" data set has the same resolution cut off but includes structures that feature bound proteins.

[2]The twist coupling was calculated from the predictions of the slope $d\Delta L/dN$ and stretch modulus S for each parameter set using **Eqn. 20**.

Table S3: Changes of average base-pair step parameters upon stretching for 100-bp dsDNA and dsRNA helices.

	Force (pN)	Avg. extension (nm)	Avg. rise (Å)[1]	Avg. roll (°)[1]	Avg. twist (°)[1]
D N A	1	28.5	3.300 / 0.006	1.56 / -0.001	35.22 / 0.004
	5	30.9	3.305 / 0.020	1.56 / -0.007	35.27 / 0.019
	10	31.6	3.310 / 0.036	1.57 / -0.005	35.33 / 0.039
	20	32.2	3.323 / 0.075	1.56 / -0.007	35.45 / 0.076
	40	32.8	3.349 / 0.153	1.55 / -0.009	35.69 / 0.152
R N A	1	24.0	3.225 / 0.002	7.85 / -0.008	31.74 / 0.008
	5	25.9	3.228 / 0.012	7.75 / -0.027	31.80 / 0.029
	10	26.6	3.230 / 0.021	7.62 / -0.055	31.88 / 0.061
	20	27.2	3.237 / 0.045	7.36 / -0.108	32.03 / 0.115
	40	27.9	3.250 / 0.093	6.90 / -0.201	32.33 / 0.226

Simulations were performed using the "2.8_noprot" parameter set. The changes of shift, slide and tilt upon stretching are small (below 0.02 standard deviations) and therefore not shown.
[1]The first value is the average parameter, followed by the corresponding Z-score.

Table S4: Effects of individual parameters in the covariance matrix for dsDNA.

	Bending persistence length (nm)	Change (%)	Torsional persistence length (nm)	Change (%)	Link vs. force slope (rad/pN)[1]	Change (%)
Original	53.0		29.0		0.226	
Shift_half[2]	53.0	0.1	28.7	-1.0	0.224	-1.1
Shift_double[2]	53.1	0.1	28.1	-3.0	0.209	-7.5
Slide_half	53.0	0.0	28.7	-1.0	0.246	8.9
Slide_double	53.0	0.0	32.0	10.3	0.200	-11.6
Rise_half	53.0	0.0	30.3	4.5	0.239	5.8
Rise_double	53.0	0.1	27.9	-3.8	0.227	0.5
Tilt_half	62.8	18.6	28.9	-0.5	0.237	4.7
Tilt_double	40.4	-23.8	28.3	-2.4	0.227	0.5
Roll_half	78.8	48.7	28.2	-2.8	0.208	-8.0
Roll_double	32.0	-39.5	29.9	2.9	0.188	-16.7
Twist_half	53.0	0.1	57.6	98.4	0.248	9.8
Twist_double	52.8	-0.3	13.3	-54.1	0.249	10.3
Shift-Slide_revsign[3]	52.9	-0.1	28.1	-3.1	0.228	0.7
Shift-Rise_revsign	53.0	0.0	28.4	-2.0	0.224	-0.8
Shift-Tilt_revsign	53.0	0.1	28.9	-0.3	0.215	-4.9
Shift-Roll_revsign	53.0	0.0	30.9	6.3	0.226	0.1
Shift-Twist_revsign	53.0	0.0	26.5	-8.5	0.216	-4.7
Slide-Rise_revsign	53.1	0.2	28.5	-1.8	0.170	-24.8
Slide-Tilt_revsign	52.9	-0.1	28.8	-0.7	0.220	-2.7
Slide-Roll_revsign	53.0	0.0	31.4	8.2	0.262	15.7
Slide-Twist_revsign	53.0	0.1	25.9	-10.9	0.177	-21.5
Rise-Tilt_revsign	53.1	0.1	30.0	3.4	0.207	-8.3
Rise-Roll_revsign	53.0	0.1	29.7	2.3	0.216	-4.3
Rise-Twist_revsign	53.0	0.0	27.1	-6.6	-0.226	-200.0
Tilt-Roll_revsign	53.1	0.1	31.0	6.9	0.229	1.4
Tilt-Twist_revsign	52.9	-0.1	28.2	-2.8	0.248	9.4
Roll-Twist_revsign	56.2	6.2	25.4	-12.5	0.234	3.4

Calculations are based on the 2.8_noprot parameter set.

[1]Here we used the slope of linking number (bead rotation) vs. stretching force to evaluate twist-stretch coupling, as this quantity is faster to evaluate in simulations than the slope of extension vs. turns at constant force.

[2]Halving or doubling the variance of 'shift' parameter in the covariance matrix.

[3]Reverse the sign of the shift-slide covariance in the covariance matrix.

Table S5: Effects of individual parameters in the covariance matrix for dsRNA.

	Bending persistence length (nm)	Change (%)	Torsional Persistence length (nm)	Change (%)	Link vs. force slope (rad/pN)[1]	Change (%)
Original	62.9		52.8		0.174	
Shift_half[2]	63.0	0.1	52.7	-0.3	0.164	-6.2
Shift_double[2]	62.9	0.0	58.8	11.3	0.161	-7.6
Slide_half	62.9	0.0	54.8	3.7	0.173	-0.9
Slide_double	62.9	0.0	52.8	-0.1	0.176	0.7
Rise_half	62.9	0.0	54.2	2.5	0.143	-17.9
Rise_double	62.9	0.0	53.7	1.6	0.152	-12.6
Tilt_half	73.7	17.1	51.3	-3.0	0.155	-10.9
Tilt_double	48.7	-22.6	53.9	2.0	0.172	-1.6
Roll_half	92.1	46.3	55.9	5.8	0.237	35.9
Roll_double	38.5	-38.7	49.3	-6.6	0.047	-73.2
Twist_half	64.0	1.7	102.9	94.8	0.122	-29.9
Twist_double	60.8	-3.3	28.0	-47.1	0.316	81.1
Shift-Slide_revsign[3]	63.0	0.1	54.0	2.3	0.161	-7.8
Shift-Rise_revsign	63.2	0.4	54.2	2.7	0.174	-0.1
Shift-Tilt_revsign	63.0	0.1	52.6	-0.4	0.151	-13.4
Shift-Roll_revsign	62.9	0.0	52.8	0.0	0.154	-11.8
Shift-Twist_revsign	62.8	-0.1	54.7	3.6	0.151	-13.3
Slide-Rise_revsign	62.9	0.1	53.5	1.3	0.174	-0.1
Slide-Tilt_revsign	62.9	-0.1	53.6	1.4	0.191	9.5
Slide-Roll_revsign	62.8	-0.2	55.5	5.0	0.166	-4.5
Slide-Twist_revsign	62.9	0.0	54.0	2.3	0.071	-59.3
Rise-Tilt_revsign	62.9	0.0	53.2	0.7	0.167	-4.3
Rise-Roll_revsign	62.8	-0.1	54.0	2.2	0.151	-13.6
Rise-Twist_revsign	62.9	0.0	54.4	3.0	0.100	-42.8
Tilt-Roll_revsign	62.9	-0.1	51.1	-3.3	0.179	2.6
Tilt-Twist_revsign	63.0	0.2	55.0	4.1	0.167	-4.0
Roll-Twist_revsign	68.0	8.0	46.3	-12.4	0.048	-72.2

Calculation are based on the 2.8_noprot parameter set.

[1]Here we used the slope of linking number (bead rotation) vs. stretching force to evaluate twist-stretch coupling, as this quantity is faster to evaluate in simulations than the slope of extension vs. turns at constant force.

[2]Halving or doubling the variance of 'shift' parameter in the covariance matrix.

[3]Reverse the sign of the shift-slide covariance in the covariance matrix.

Table S6. Original and refitted variance and covariance parameter sets for dsDNA and dsRNA simulations.

|	DNA_2.8 _all	DNA_2.8 _noprot	DNA_refit	RNA_2.8 _all	RNA_2.8 _noprot	RNA_refit
shift[1]	0.64	0.58	0.58	0.66	0.57	0.57
slide[1]	0.82	0.86	0.86	0.44	0.39	0.39
rise[1]	0.25	0.23	0.33	0.24	0.20	0.29
tilt[1]	3.85	3.58	3.58	3.52	2.87	2.87
roll[1]	6.25	5.19	5.92	5.2	4.33	4.94
twist[1]	5.43	6.27	3.14	4.73	4.25	2.69
shift-slide[2]	0.02	0.02	0.02	-0.01	0.03	0.03
shift-rise[2]	-0.02	-0.03	-0.02	0.01	-0.01	-0.01
shift-tilt[2]	0.34	0.27	0.27	0.25	0.36	0.36
shift-roll[2]	0	0.01	0.01	0.01	0.02	0.02
shift-twist[2]	0.01	-0.04	-0.08	0.03	-0.01	-0.01
slide-rise[2]	-0.07	0.11	0.08	-0.23	-0.19	-0.13
slide-tilt[2]	0.01	-0.01	-0.01	-0.07	0.00	0.00
slide-roll[2]	-0.17	-0.09	-0.08	0.13	0.10	0.08
slide-twist[2]	0.4	0.25	0.49	0.39	0.40	0.64
rise-tilt[2]	-0.01	0.05	0.03	0.03	-0.03	-0.02
rise-roll[2]	0.03	-0.16	-0.10	0.23	0.17	0.11
rise-twist[2]	0.26	0.37	0.16	0.1	0.11	-0.12
tilt-roll[2]	-0.02	-0.01	-0.01	-0.01	0.01	0.01
tilt-twist[2]	0	0.02	0.05	-0.07	-0.02	-0.02
roll-twist[2]	-0.42	-0.42	-0.73	-0.1	-0.13	0.09

[1]The standard deviation of shift, slide, rise, tilt, roll, twist. Units for shift and slide and rise are Å and units for tilt, roll and twist are degree.
[2]The correlation coefficient (unit-less) for shift vs. slide and so on.

Table S7: Mechanical properties from the modified parameter sets.

Parameter	Symbol (units)	dsRNA		dsDNA	
		2.8_noprot	modified	2.8_noprot	modified
Bending persistence length	A (nm)	66.3	59.9	54.7	47.0
Stretch modulus	S (pN)	979	685	1956	1067
Torsional persistence length	C_{lim} (nm)	53.0	103.7	28.8	124.8
Slope of the extension vs. turns response close to zero turns	$d\Delta L/dN$ (nm/turn)	0.797	-0.832	0.473	0.599
Twist-stretch coupling	D (unitless)	-30.3	22.1	-35.9	-24.8

SUPPLEMENTARY FIGURES
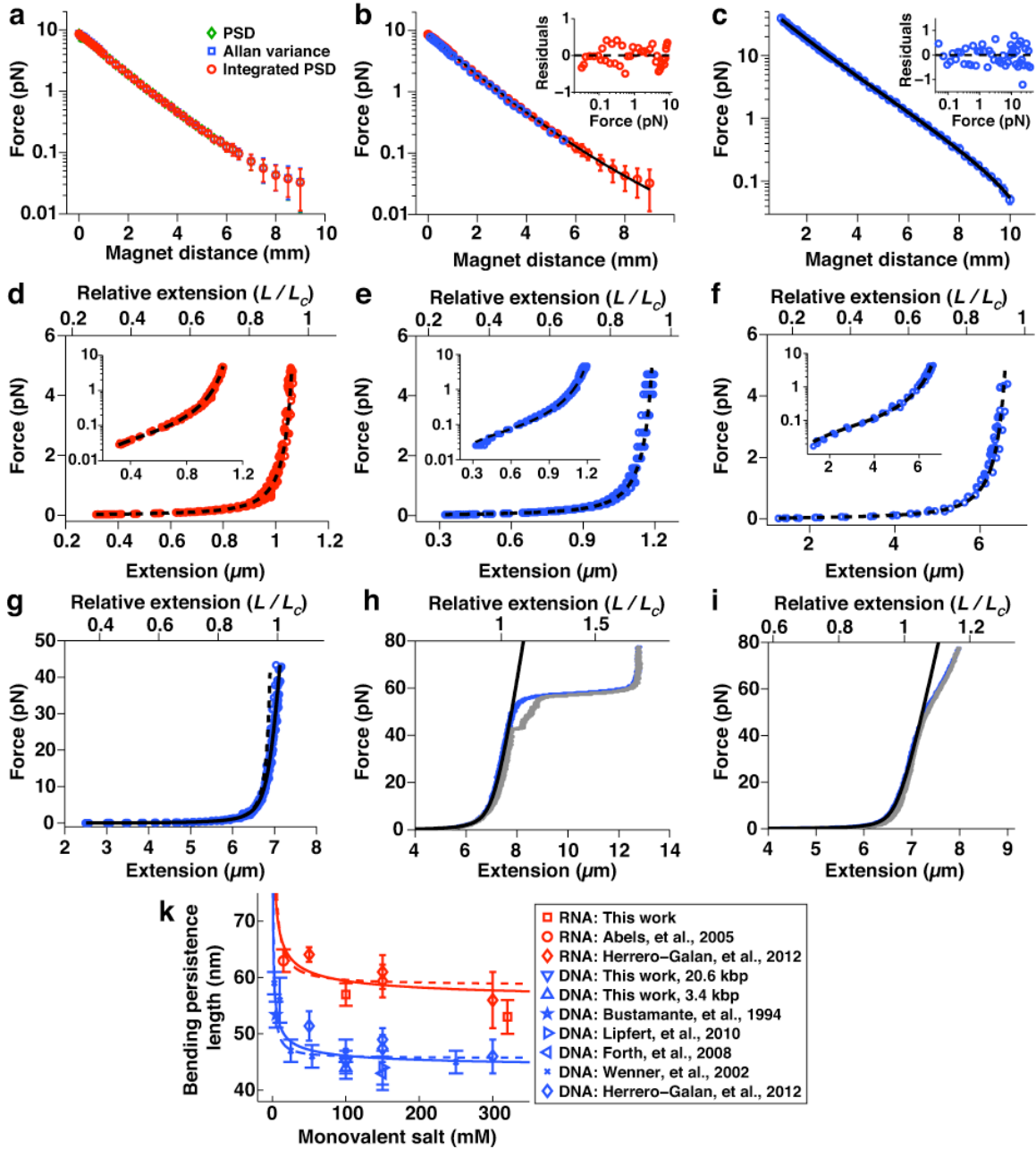
Fig. S1. Force calibration and stretching experiments on dsRNA and dsDNA in the magnetic tweezers.

a) Force calibration including spectral corrections. Comparison of different methods to determine the applied stretching forces in the MT from the position fluctuations of the magnetic beads. Data were obtained using MyOne beads and 4.2 kbp dsRNA tethers with a set of vertically-oriented magnets with a 1 mm gap. Points are the mean and standard deviation from 16 independent tethers. The same experimental data were analyzed using three different methods to determine the stretching forces (see also the "Force calibration in the magnetic tweezers" section): 1) by fitting of the power spectral density using the

method by Lansdorp and Saleh (11) (green diamonds), 2) from an analysis of the Allan variance of the data (11) (blue squares) , and 3) by fitting the integral of the power spectral density of the data (10) (red circles). The three methods yield identical results, within experimental error. Note that symbols partially overlap. All force values reported below were obtained by fitting the integral of the power spectral density.

b) Force calibration for MyOne beads. The applied stretching force as a function of the distance Z_{mag} between a set of vertically-oriented magnets with a 1 mm gap and the flow-cell surface for MyOne beads. Data for 4.2 kbp dsRNA tethers (red symbols; points are the mean and standard deviation σ from 16 independent tethers) agree within experimental error with data obtained previously (2) using 20.6 kbp DNA tethers (blue circles). The RNA data were fit to an empirical double exponential model of the form $F(Z_{mag}) = \alpha_1 \cdot \exp(-Z_{mag} / \xi_1) + \alpha_2 \cdot \exp(-Z_{mag} / \xi_2)$ to provide a convenient conversion from magnet position to force. The fit (black line) yielded fitting parameters: $\alpha_1 = 8.0$ pN, $\xi_1 = 1.23$ mm, $\alpha_2 = 0.76$ pN, and $\xi_2 = 2.48$ mm. The inset shows the residuals between the fit and the RNA data, defined as $(F_{data} - F_{fit}) / \sigma_{data}$.

c) Force calibration for M270 beads. The applied stretching force as a function of the distance Z_{mag} between a set of vertically-oriented magnets with a 1 mm gap and the flow-cell surface for M270 beads. The dataset was obtained using 20.6 kbp DNA tethers; symbols are the mean and standard deviation from ten independent tethers. The data were fit to an empirical piece-wise exponential model of the form $F(Z_{mag}) = \alpha_{high} \cdot \exp(-Z_{mag} / \xi_{high}) + \delta_{high}$ for $F > 5$ pN and an analogous expression for $F < 5$ pN with fitting parameters α_{low} , ξ_{low} , and δ_{low}. The fit (black line) to the experimental data yielded fitting parameters: $\alpha_{high} = 76.83$ pN, $\xi_{high} = 1.36$ mm, $\delta_{high} = 0.64$ pN, $\alpha_{low} = 61.61$ pN, $\xi_{low} = 1.55$ mm, and $\delta_{low} = -0.04$ pN. The inset shows the residuals between the fit and the measured data, defined as in panel a. All data shown were obtained in TE buffer with 100 mM NaCl added.

d) Force-extension measurements for 4.2 kbp RNA at high salt. Force-extension relationship for a 4.2 kbp dsRNA in TE buffer with 320 mM NaCl added (symbols), together with a fit to the inextensible WLC model (dashed line). The inset shows the same data with a logarithmically scaled force axis. From fits of the WLC model to several such measurements, we find $A_{RNA} = 53 \pm 3$ nm (mean and SEM from measurement on 6 independent molecules).

e) Force-extension measurements for 3.4 kbp DNA. Force-extension relationship for a 3.4 kbp dsDNA tether in TE buffer with 100 mM NaCl added (symbols) together with a fit to the inextensible WLC model (dashed line). The inset shows the same data with a logarithmically scaled force axis. From fits of the WLC model we find $A_{DNA} = 44 \pm 2$ nm (mean and SEM from measurement on 5 independent molecules).

f) Force-extension measurements for 20.6 kbp dsDNA. Low force force-extension curves for a 20.6 dsDNA tether in TE buffer with 100 mM NaCl added (symbols) and fit of the inextensible WLC model (dashed line). The inset shows the same data with a logarithmically scaled force axis. From fits of the WLC model we find $A_{DNA} = 44 \pm 2$ nm (mean and SEM from measurement on 8 independent molecules).

g) High force force-extension curves for a 20.6 kbp dsDNA in TE buffer with 100 mM NaCl added (symbols) and fit of the extensible WLC model (solid line), which gives a stretching modulus of $S_{DNA} = B_{DNA} \cdot k_B T \sim 1000$ pN, in agreement with previously

determined values (23, 27, 75, 76). The inextensible WLC model (fit to the data with $F <$ 5 pN) is shown for comparison (dashed line).

h) Overstretching measurement for nicked dsDNA. Dynamic force-spectroscopy measurements (12) of torsionally unconstrained dsDNA. Stretching (blue) and release (grey) traces are shown separately and reveal some hysteresis. The data < 50 pN are well-described by the extensible WLC model (black solid line). At higher forces the overstretching transition is readily apparent (see discussion below).

i) Overstretching measurement for torsionally constrained dsDNA. Dynamic force-spectroscopy measurements of torsionally constrained dsDNA (color-code as in panel h). For torsionally constrained dsDNA, the overstretching transition is not marked by a sharp plateau (as seen in panel h) and occurs much more gradual, in agreement with previous findings (see discussion below). All overstretching data shown were obtained in TE buffer with 100 mM NaCl added.

k) Salt dependence of the bending persistence length *A* for dsRNA and dsDNA as a function of monovalent salt concentration. Values for A_{RNA} were obtained in this work (**Fig. S2** and panel d) and taken from Abels, *et al. (22)* (red circle) and Herrero-Galan et al. (23) (red diamonds). Values for A_{DNA} were obtained in this work (panels e and f; blue triangles); additional literature values were taken from Bustamante, *et al. (19)* (blue star), Lipfert, *et al. (13)* (blue right-pointing triangle), Forth, *et al. (34)* (blue left-pointing triangle) and Wenner, *et al. (75)* (blue crosses), and Herrero-Galan *et al.* (23) (blue diamonds). To describe the salt dependence of the bending persistence lengths, we fit models to the combined data that describe the bending persistence length as a sum of a salt independent contribution A_0 and a salt dependent contribution: $A = A_0 + m \,[\text{salt}]^C$. The scaling parameter is $C = -1$ in the model by Odijk (77) and Skolnick and Fixman (78) and $C = -0.5$ in the model due to Barrat and Joanny (79). [salt] is the monovalent salt concentration and A_0 and m were treated as free fitting parameters. Both the dsRNA and dsDNA data are almost equally well described by the two models. Employing the Odijk and Skolnick-Fixman model (dashed lines), we found for dsRNA $A_{0,RNA} = 58.6$ nm, $m = 95.5$ nm·mM (reduced $\chi^2 = 2.11$; dashed red line) and for dsDNA $A_{0,DNA} = 45.7$ nm, $m = 38.5$ nm·mM (reduced $\chi^2 = 0.91$; dashed blue line). Fitting the model due to Barrat and Joanny (solid lines), we found for dsRNA $A_{0,RNA} = 55.4$ nm, $m = 40$ nm·mM (reduced $\chi^2 = 1.63$; solid red line) and for dsDNA $A_{0,DNA} = 43.6$ nm, $m = 25.2$ nm·mM (reduced $\chi^2 = 0.63$; solid blue line).

Overstretching transition for dsRNA and dsDNA. Since its first observation in single-molecule stretching experiments (56, 76), the overstretching transition of dsDNA has been studied extensively. In brief, torsionally unconstrained dsDNA molecules lengthen to ~1.7 times their contour length (56, 76) over a narrow force range at ~60 pN. The value of the force at which the overstretching plateau occurs has been shown to decrease with decreasing ionic strength (27, 75, 76), to decrease with increasing temperature (80), to decrease with decreasing GC-content (81), and to decrease when the pH is reduced below pH 4 or increased above pH 10 (Ref. (82)). There has been a debate on the molecular basis of the overstretching transition. While some authors have argued that B-form DNA converts to an alternative, stretched but still double-stranded conformation termed S-DNA at the overstretching transition (56), followed by melting at significantly higher forces (81), others have argued that the overstretching transitions involves at least partial separation of the DNA strands (75, 76, 80, 82). In particular, the results of

overstretching experiments in the presence of glyoxal (83) and of fluorescence microscopy visualization experiments on stretched molecules (84, 85) have been interpreted in favor of DNA melting at the overstretching transition. Recently, several studies have carefully revisited the problem and have argued in favor of two distinct overstretched states in DNA, melting and an alternative S-form DNA, that depend on temperature, salt concentration, and sequence composition (86-90). The sharp overstretching transition at ~ 60 pN is abolished if the dsDNA molecule is fully torsionally constrained, i.e. free of internal nicks and attached via multiple attachment points at both ends (panel d and Refs. (84, 91, 92)). Torsionally constrained dsDNA molecules undergo a much more gradual overstretching transition, compared to torsionally unconstrained molecules, extending by < 20% under forces of >100 pN (Refs. (84, 92)).

In contrast to dsDNA, much less is known about the overstretching behavior of dsRNA. A study employing an atomic force microscopy tip to stretch dsRNA relying on unspecific attachment found an overstretching transition qualitatively similar to that observed in dsDNA (93). The results indicated that dsRNA lengthens by 2.0 ± 0.2 fold, compared to the 1.7-fold lengthening of dsDNA, and found overstretching forces in the range of 50-80 pN. Comparing two dsRNA constructs with different GC-contents, the overstretching force was larger for the construct with higher GC-content. Comparing dsRNA constructs to dsDNA constructs with the same GC-content, the overstretching force was larger for dsRNA than for dsDNA. A recent study observed the dsRNA overstretching transition employing optical tweezers (23); it found a similar relative length increase for dsRNA and dsDNA upon overstretching, lower overstretching forces for dsRNA compared to dsDNA, and a decrease in overstretching forces with decreasing salt concentrations.

For torsionally unconstrained dsRNA, we observed a sharp overstretching transition where dsRNA lengthened to 1.8 ± 0.1 times its contour length; this result is intermediate to and in agreement, within experimental error, with the two previous reports (23, 93). We found lower overstretching forces for dsRNA than for dsDNA of similar GC-content, in agreement with the results of Herrero-Galán (23). In addition, we also observed decreasing overstretching forces with decreasing ionic strength (**Fig. S2c**, inset). The characteristic overstretching force for torsionally unconstrained dsRNA increased from 51 ± 5 to 54 ± 5, and 61 ± 8 pN at 50, 100, and 500 mM NaCl, respectively, while the length increase was independent of salt concentration.

 The fact that the overstretching force increases with increasing salt concentration suggests that the spacing between the negatively charged phosphate groups increases upon overstretching, which is therefore favored by lower ionic strength conditions. This behavior is consistent with RNA melting upon overstretching, however, it is also possible that RNA (at least partially) adopts an alternatively structure upon overstretching that we tentatively call S-RNA, in analogy to S-DNA.
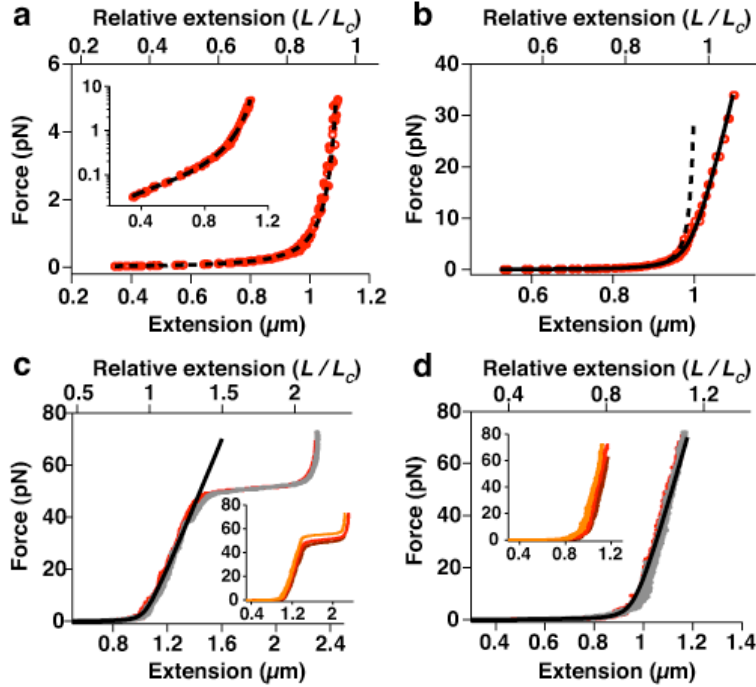
Fig. S2. (Over-)stretching measurements on 4.2 kbp double-stranded RNA.
a) Low force force-extension curves for dsRNA (symbols) and fit of the inextensible WLC model (dashed line). The inset shows the same data with a logarithmically scaled force axis. **b)** High force force-extension curves for dsRNA (symbols) and fit of the extensible WLC model (solid line). The inextensible WLC model is shown for comparison (dashed line). Data in panel a and b are in the presence of 100 mM NaCl. **c)** Dynamic force-spectroscopy measurements (12) (see Methods) of torsionally unconstrained dsRNA. Stretching (red) and release (grey) traces are shown separately and reveal some hysteresis. The data < 40 pN are well-described by the extensible WLC model (black solid line), at higher forces the overstretching transition is readily apparent. The inset compares stretching measurements performed in TE buffer with 50 (brown), 100 (red), and 500 (orange) mM NaCl added. **d)** Dynamic force-spectroscopy measurements of torsionally constrained dsRNA. Color-code is the same as panel c). For torsionally constrained dsRNA, no overstretching is observed up to 75 pN.
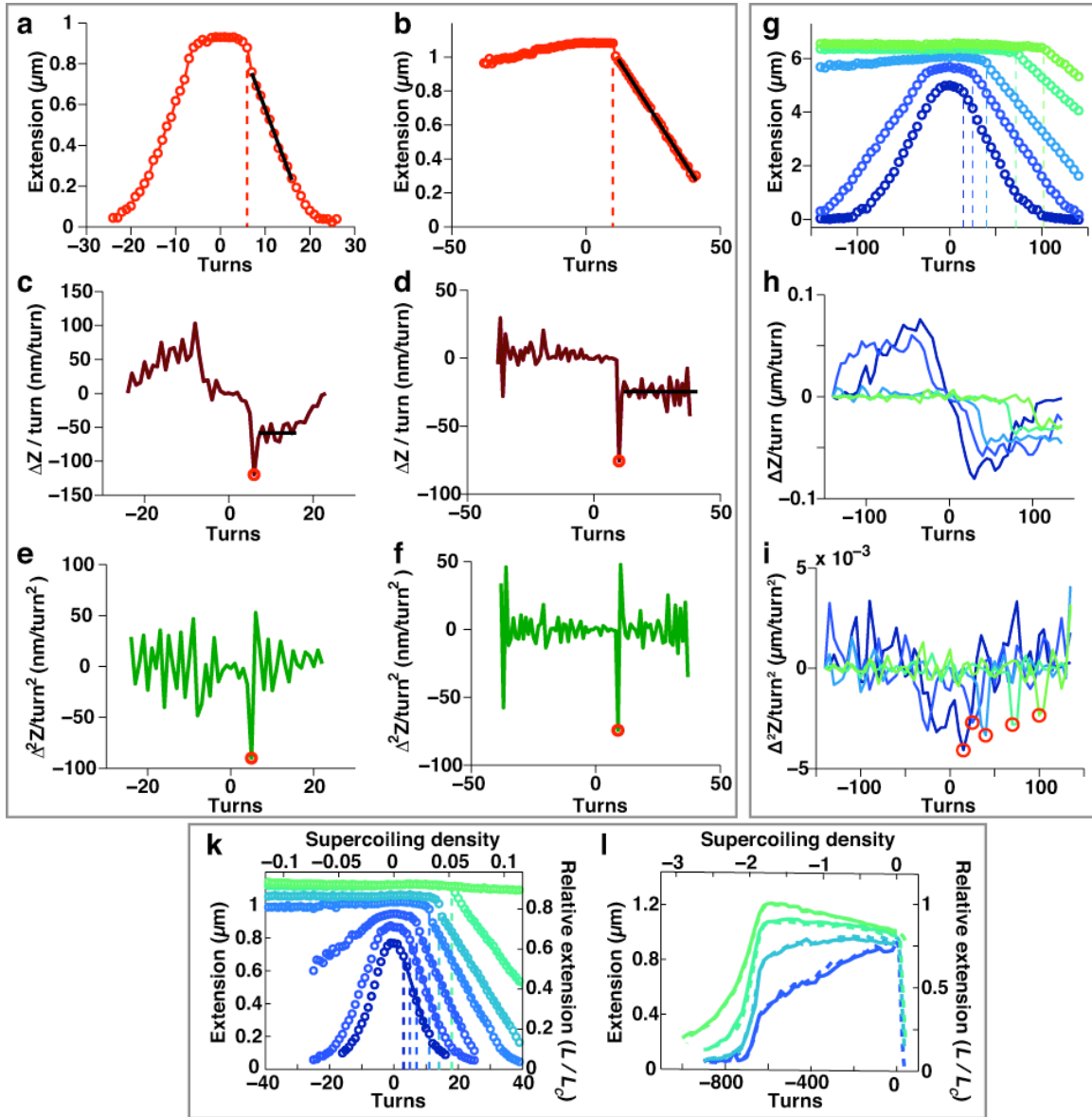
Fig. S3. Analysis of rotation-extension measurements for dsRNA and dsDNA.
a-f) Determination of the buckling points and the slopes in the plectonemic region
for dsRNA. a,b) Example rotation-extension curves for 4.2 kbp dsRNA at stretching
forces of 0.5 pN (panel a) and 3 pN (panel b). The buckling points (indicated by vertical
dashed lines) were determined from the second derivative of the rotation-extension data
as described below. The slopes in the plectonemic regime were determined by linear fits
of the rotation-extension data (indicated by solid black lines) beyond the buckling points.
The fitting range for the linear fit was set manually, taking into account the first
derivative (see below), limiting the fit to the linear region beyond the buckling point, and
excluding data too close to the surface (typically data with an extension < 0.2 μm is
excluded). **c,d)** First derivatives of the extension with respect to the applied number of
turns for the $F = 0.5$ pN data (panel c) and the $F = 3$ pN data (panel d). The first

29

derivatives were computed as a finite difference ΔZ / turn = $(Z[n_{i+1}] - Z[n_i])$ / $(n_{i+1} - n_i)$, where $Z[n_i]$ is the extension at n_i turns. For the RNA rotation curves, the first derivative tends to exhibit a minimum that could be identified with the buckling point (indicated by a red circle); however, we found it to be more robust to determine the buckling point from the second derivative of the data, see below. In addition, the first derivative takes on approximately constant negative values (black lines) in the plectonemic region that was used to determine the slope in panels a and b. **e,f)** Second derivatives of the extension with respect to the applied number of turns for the $F = 0.5$ pN data (panel e) and the $F = 3$ pN data (panel f). The second derivatives were computed as $\Delta^2 Z$ / turn^2 = $(\Delta Z[n_{i+1}] - \Delta Z[n_i])$ / $(n_{i+1} - n_i)$ and the minimum of the second derivative at positive turns n_{min} was determined (red circles). The buckling point was taken to be the point n_{min+1} (red vertical lines in panel a and b).

g)-i) Rotation-extension curves and determination of the buckling points for dsDNA. g) Rotation-extension curves for 20.6 kbp DNA at forces of 0.25, 0.5, 1, 3, and 5 pN (color coded from dark to light). Buckling points were determined from the second derivative of the extension with respect to the number of applied turns, as described above and are indicated by vertical dashed lines. **h)** First derivatives of the extension with respect to the applied number of turns of the data in panel g. **i)** Second derivatives of the extension with respect to the applied number of turns of the data in panel g. The buckling points are determined by finding the minima of the second derivatives (indicated by red circles) as described above.

k)-l) Response of 3.4 kbp dsDNA to changes in linking number at various stretching forces and formation of L-DNA. k) Rotation-extension curves for 3.4 kbp dsDNA at different stretching forces (0.25, 0.5, 1, 2.75, 4.75, and 6.5 pN, color coded from dark blue to lighter green). The top axis shows the supercoiling density, $\sigma = \Delta Lk/Lk_0$, where Lk_0 is the linking number of torsionally relaxed dsDNA. Dashed lines denote the buckling points at positive turns and solid lines linear fits to the extension in the plectonemic region (determined as described above). **l)** Rotation-extension curves for 3.4 kbp dsDNA out to large negative σ at $F = 2, 3, 4,$ and 6 pN (dark blue to lighter green). Solid lines are for unwinding, dashed lines are for subsequent rewinding; the rotation-extension behavior for large negative σ is discussed in more detail below. All data presented were obtained in TE buffer in the presence of 100 mM NaCl. *Highly underwound dsRNA and dsDNA.* Unwinding of dsDNA at stretching forces above ~ 1 pN leads to denaturation or melting of the dsDNA (94). Continued unwinding in this regime initially leads to the denaturation of additional base pairs, while the tether extension remains approximately constant (panel l and Ref. (91, 94)). An abrupt change in the extension at a supercoiling density of σ ~ -1.8 denotes the onset of a transition to new state of dsDNA, termed L-DNA (panel l and Ref. (33, 95)). L-DNA has a negative helicity of ~ -13 bp/turn and has been found to be more flexible and to have a longer contour length than B-form dsDNA (33, 95). If the unwinding was carried at relatively low forces, below ~ 3 pN, the extension was somewhat variable as unwinding proceeded and exhibited hysteresis upon rewinding (panel l), possibly due to the formation of secondary structure, in agreement with previous findings (95).

We observed an overall similar behavior for dsRNA upon unwinding at stretching forces above ~ 1 pN. An abrupt change of the extension at σ ~ -1.9 marks the formation of a new state of dsRNA that we term L-RNA, in analogy to L-DNA (**Fig. 2d**). Our

measurements indicate that L-RNA has a negative helicity of -12.6 bp/turns and is elongated with respect to A-form dsRNA. Similar to dsDNA, we observe a more variable extension and hysteresis upon rewinding at forces below ~ 3 pN (**Fig. 2d**), which again might possibly due to the formation of local secondary structure.
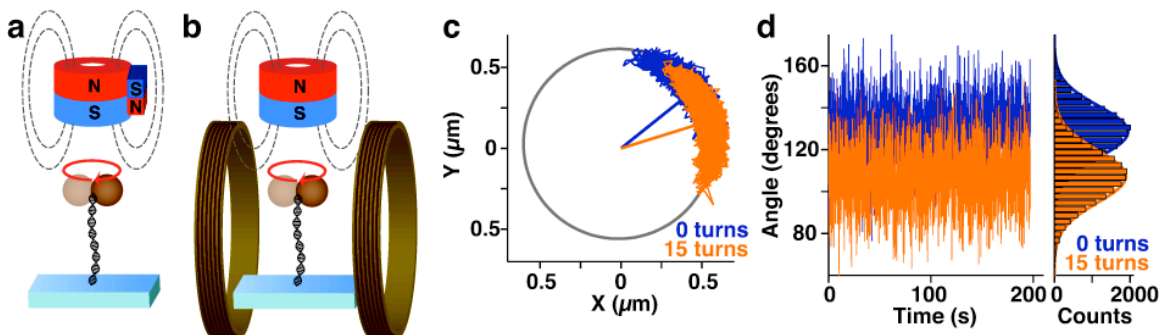
Fig. S4. Schematic of torque measuring magnetic tweezers and principle of angular tracking.
a) Schematic of magnetic torque tweezers (MTT), a variant of magnetic tweezers that uses a cylindrical magnet with a small side magnet to apply stretching forces and enable the application and measurement of torque. **b)** Schematic of electromagnetic torque tweezers (eMTT) that use a vertically aligned cylindrical magnet to apply forces and two pairs of Helmholtz coils (only one pair is shown in the schematic for clarity) to apply small horizontal fields to permit the application and measurement of torque about the tether axis (14). **c)** (x,y)-position fluctuations of a MyOne bead tethered to a 4.2 kbp dsRNA tether held in the eMTT at 0 turns (blue data), corresponding to a torsionally-relaxed tether; and after rotating the bead for 15 turns (orange data). The grey circle indicates the circle fitted to the overall (x,y)-position fluctuations that lie on a circular annulus (16). A shift in the position fluctuation after applying 15 turns is apparent. The solid blue and orange lines indicate the mean angular position for each data set. **d)** Rotation angle as a function of time deduced from the (x,y)-position data in panel c. The panel at right shows the corresponding histograms of the rotation angle. The fluctuations are well described by a Gaussian fit (solid lines) with a standard deviation of ~12°, corresponding to a trap stiffness of ~90 pN·nm/rad. A shift in the mean angle between 0 and 15 applied turns due to the restoring torque exerted by the RNA tether is evident.
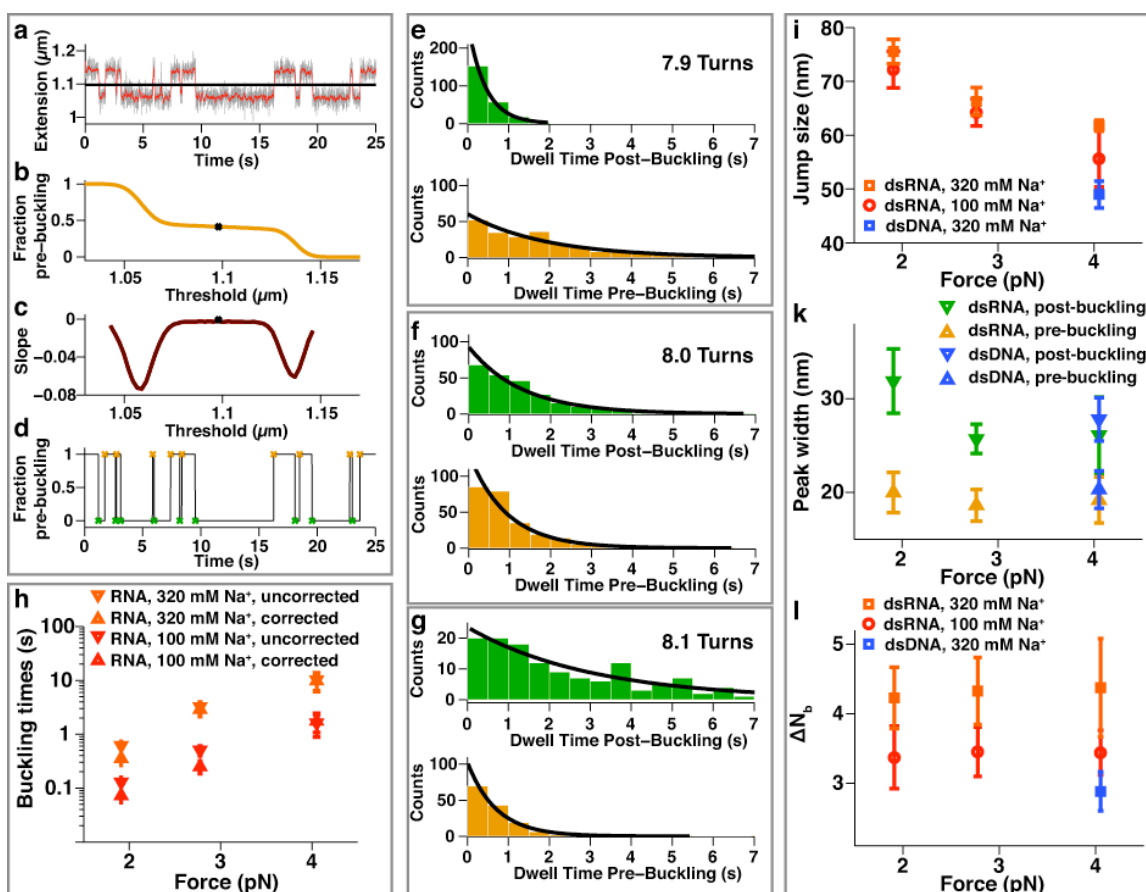
**Fig. S5. Analyses of extension vs. time traces at the buckling transition.**
**a)-d) Illustration of the threshold selection to determine the pre- and post-buckling
states from extension vs. time traces. a)** Example of an extension vs. time trace for
dsRNA at the buckling transition. Raw data acquired at 120 Hz are shown in grey, data
filtered at 20 Hz are shown in red. The best threshold as determined by the algorithm
described below is shown as a black vertical line. **b)** Fraction of the points in the pre-
buckling ("up") state as a function of the threshold position. **c)** First derivative of the
fraction pre-buckling vs. threshold position data in panel b. Our algorithm to find an
optimal threshold is based on systematically using "trial thresholds" to partition the data
into a pre- ("up") and post-buckling ("down") states. We determine the optimal threshold
by selecting the threshold value that has the smallest absolute slope in the fraction pre-
buckling vs. threshold position plot (indicated by a black crosses in panel b and c). **d)**
Partitioning of the data trace in panel a into pre- and post-buckled states using the optimal
threshold. Time points where a transition from the post- to the pre-buckled state ("0 to
1") occur are indicated by green crosses, transition from the pre- to the post-buckled state
("1 to 0") are marked by dark yellow crossed. The time points of the transition are used to
determine the dwell time distributions of the pre- and post-buckling states.
e)-g) Examples of dwell-time distributions for the pre- and post-buckling states.
Dwell-time distribution for the post-buckling state (upper panels, green data) and for the
pre-buckling state (lower panels, dark yellow data) determined from extension vs. time

33

traces of a 4.2 kbp dsRNA tether at the buckling transition, for increasing number of applied turns. **e)** Dwell time histograms for the trace at 7.9 turns shown in **Fig. 5a**. The dwell-time distributions are well described by an exponential distribution (black lines) with characteristic dwell times of $\tau_{post\text{-}buckling} = 0.43$ s and $\tau_{pre\text{-}buckling} = 1.91$ s. Note that the exponential distribution was fit to the unbinned data using a maximum likelihood fit; the dwell time histograms are only shown for the purpose of graphical representation. **f)** Same as panel e, except data are at 8.0 turns and the exponential fits yield characteristic dwell times of $\tau_{post\text{-}buckling} = 1.31$ s and $\tau_{pre\text{-}buckling} = 0.93$ s. **g)** Same as panel e, except data are at 8.1 turns and the exponential fits yield characteristic dwell times of $\tau_{post\text{-}buckling} = 3.1$ s and $\tau_{pre\text{-}buckling} = 0.71$ s. As more turns are applied, the RNA spends more time in the post-buckling state and $\tau_{post\text{-}buckling}$ increases while $\tau_{pre\text{-}buckling}$ decreases (see also **Fig. 5c**). Data were obtained in TE buffer with 320 mM NaCl added.

h) Characteristic buckling times with corrections for finite camera acquisition rate. Characteristic dwell times at the buckling transitions for 4.2 kbp dsRNA obtained from fitting the dwell times of the pre- and post-buckling states (downward pointing triangles; these are the dsRNA data shown in **Fig. 5e**) and the characteristic dwell times obtained by first applying a correction for finite sampling frequency to the dwell times of the pre- and post-buckling states (upward pointing triangles). See the "Two-state model of the buckling transition" section for details of the correction procedure.

i)-l) Analysis of the extension jumps at the buckling transition. i) Size of the jump in extension upon buckling as a function of stretching force for 4.2 kbp dsRNA in TE buffer with 100 mM (red circles) and 320 mM (orange squares) NaCl added. For comparison, data for 3.4 kbp dsDNA in TE buffer with 320 mM NaCl are shown (blue square). The jump size was determined by fitting the extension histograms with a double Gaussian (**Fig. 5a**) and taking the peak-to-peak distance. We observe a small, but systematic change in the size of the extension jump at different numbers of applied turns across the buckling transition (similar to what has been observed in Ref. (96)). For the current analysis, we used the value for the trace closest to the point where the pre-buckling fraction is 0.5 for each data set. Points are the mean and SEM from at least four independent measurements. Our data point for dsDNA is consistent, within experimental error, with the data of Brutzer *et al. (51)* and of Forth *et al. (34, 97)* obtained with DNA constructs of different lengths. **k)** Width of the extension fluctuations for 4.2 kbp dsRNA and 3.4 kbp dsDNA. Data are determined by fitting a double Gaussian to the extension histograms and reporting the standard deviations for the pre-buckling peak (dark yellow triangles) and post-buckling peak (dark green triangles). Points are the mean and SEM from at least four independent measurements. Since we did not observe a significant salt dependence of the width, we only report the values at 320 mM NaCl. **l)** Number of turns converted from twist to writhe at the buckling transition, ΔN_b, for 4.2 kbp dsRNA and 3.4 kb dsDNA (same color code as in panel a). ΔN_b was determined by fitting a two-state model to the fraction post-buckling vs. turns data (**Fig. 5b** and **SI Materials and Methods**). Points are the mean and SEM from at least four independent measurements. Our data point for dsDNA is consistent, within experimental error, with the data of Brutzer *et al. (51)* obtained with DNA constructs of different lengths.
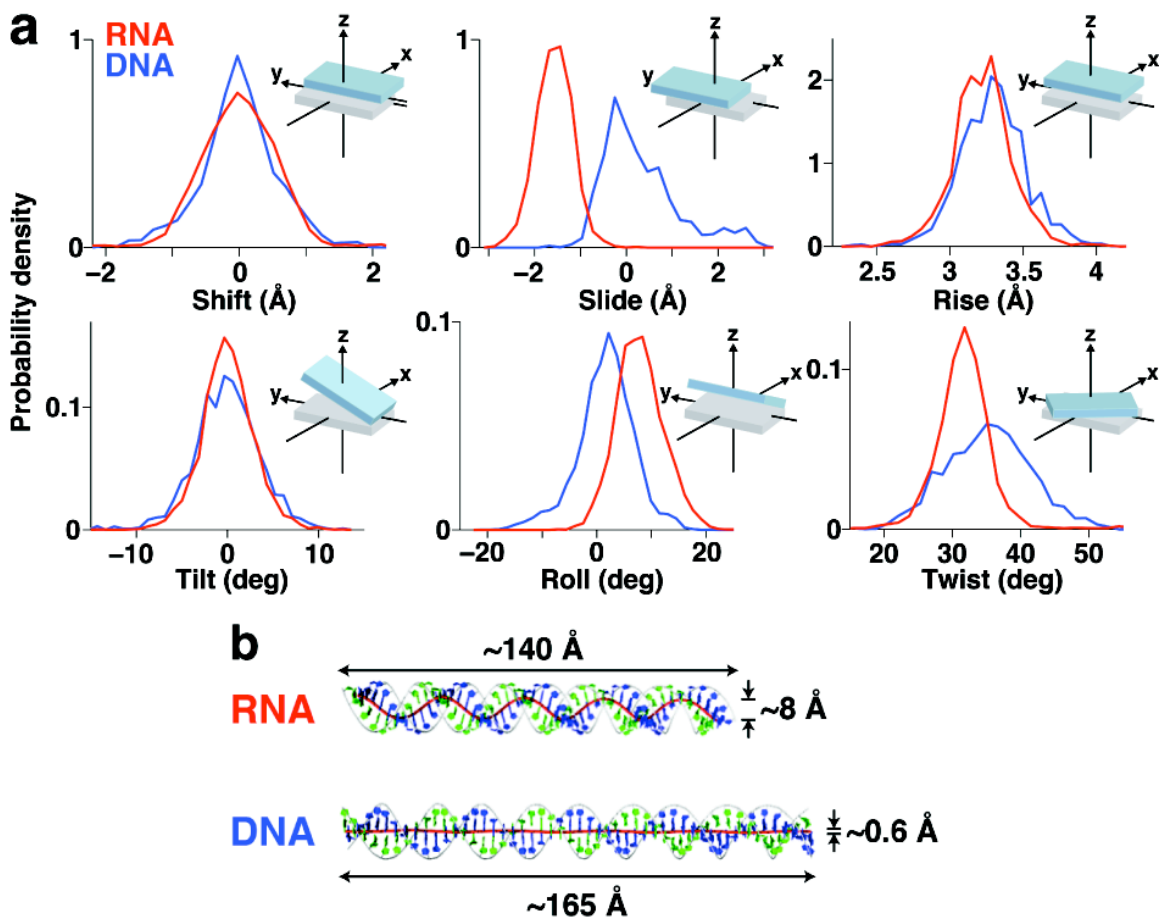
Fig. S6. Base-step parameter modeling for dsDNA and dsRNA.
a) Probability density distributions for the six base-step parameters shift, slide, rise, tilt, roll, and twist for dsRNA (red) and dsDNA (blue) extracted from analysis of crystal structures. The base-step parameters are schematically illustrated in the insets. The parameter distributions shown were obtained from crystal structures of nucleic acids deposited in the protein data bank (http://www.rcsb.org/pdb/) that had a resolution better or equal to 2.8 Å and did not contain bound proteins using the program 3DNA (67). The distributions are normalized to unit area.
b) Visualization of base-step parameter based models. Rendering of idealized 50 bp dsRNA (top) and dsDNA (bottom) helices that have all base step parameters set to their average values. The helix centerlines are shown as a dark red tube in both models. The difference in helical rise per base pair for dsRNA and dsDNA is apparent from the different lengths of the two structures. In addition, the "springiness" of the dsRNA centerline, tracing out a helix with a diameter of ~8 Å, can be compared to the almost straight centerline for dsDNA.
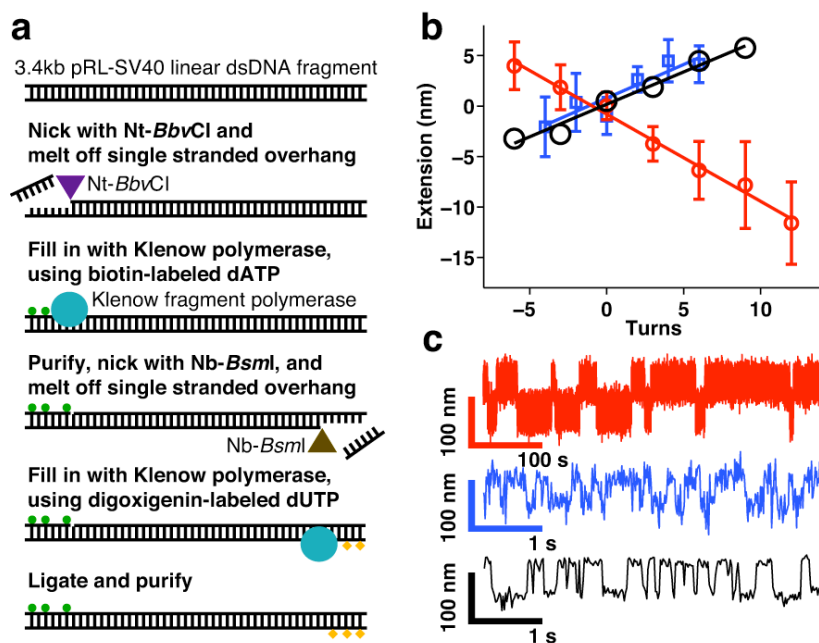
Fig. S7. Control measurements with a dsDNA construct labeled on only one strand at each end. a) Schematic of the alternative labeling procedure based on Klenow fragment polymerase fill-in reactions with labeled nucleotides. For details, see the "*Double-stranded DNA constructs with labels on only one strand at each end*" section in the Supplementary Methods. In brief, starting with a modified version of a linearized 3.4 kbp segment of the pRL-SV40 plasmid, overhangs are generated in subsequent reactions by nicking one strand and melting away the remaining 42 bp single-stranded fragment. The overhangs are filled in using Klenow fragment DNA polymerase in reactions that have one of the four nucleotides modified with biotin or digoxigenin, respectively. Finally, the remaining nicks are ligated. The resulting construct carried multiple labels on only one strand at each end, similar to our dsRNA labeling procedure.
b) Measurement of the twist-stretch coupling for the alternatively labeled dsDNA construct (large black circles) generated as described in panel a); for comparison results for dsRNA (red circles; same data as **Fig. 4b**) and conventional dsDNA employing PCR-generated labeled segments with multiple labels on both strands at both ends (blue squares; same data as **Fig. 4b**) are shown. The slope observed for the alternatively labeled dsDNA construct is $(d\Delta L/dN)_{alt.DNA} = 0.43 \pm 0.12$ nm/turn (mean $\pm$ s.e.m. from 20 measurements), which is identical, within experimental error, to the slope determined for the conventionally labeled dsDNA constructs.
c) Extension vs. time traces at the buckling transition for dsRNA (red; same data as **Fig. 5d**), conventionally labeled dsDNA (blue; same data as **Fig. 5d**), and the alternatively labeled dsDNA molecule generated as described in panel a) (black). All measurements are taken at $F = 4$ pN in TE buffer with 320 mM NaCl added. The slightly different noise characteristics for the alternatively labeled dsDNA data result from the fact that these data were recorded at 60 Hz (as opposed to the top two traces, which were acquired at 120 Hz) and used different illumination and camera settings. It is apparent that the alternatively labeled dsDNA construct undergoes transitions on a time scale very similar

36

to the conventionally labeled dsDNA and on a much slower time scale than dsRNA (note the different time axis scales for dsDNA vs. dsRNA).

From systematic analysis of time traces recorded at different number of applied turns across the buckling transition using the same procedures used to analyze the dsRNA and conventionally labeled dsDNA data, we determined the buckling time τ_{buck} for the alternatively labeled dsDNA to be 78 ± 30 ms and the number of turns converted from twist to writhe at the buckling transition ΔN_b to be 2.4 ± 0.5 at $F = 4$ pN and in TE buffer with 320 mM NaCl added (mean $\pm$ s.d. for 5 molecules). The measurements for τ_{buck} and ΔN_b for the alternatively labeled dsDNA construct are in agreement, within experimental error, to the values obtained for conventionally labeled dsDNA; for both sets of dsDNA data, the τ_{buck} estimates are upper limits, as the finite camera acquisition frequency limits our temporal resolution.

In summary, we found no difference between conventionally labeled dsDNA molecules and dsDNA molecules with labels on only on strand at each end, suggesting that the surface and bead attachment protocol does not contribute to the surprising differences in twist-stretch coupling and buckling dynamics observed between dsDNA and dsRNA.

SUPPLEMENTARY REFERENCES

1.   Lipfert J, Koster DA, Vilfan ID, Hage S, & Dekker NH (2009) Single-molecule magnetic tweezers studies of type IB topoisomerases. *Methods Mol Biol* 582:71-89.
2.   Lipfert J, Hao X, & Dekker NH (2009) Quantitative modeling and optimization of magnetic tweezers. *Biophys J* 96(12):5040-5049.
3.   Lipfert J, Klijnhout S, & Dekker NH (2010) Torsional sensing of small-molecule binding using magnetic tweezers. *Nucleic Acids Res* 38(20):7122-7132.
4.   Crut A, Nair PA, Koster DA, Shuman S, & Dekker NH (2008) Dynamics of phosphodiester synthesis by DNA ligase. *Proc Natl Acad Sci U S A* 105(19):6894-6899.
5.   Koster DA, Croquette V, Dekker C, Shuman S, & Dekker NH (2005) Friction and torque govern the relaxation of DNA supercoils by eukaryotic topoisomerase IB. *Nature* 434(7033):671-674.
6.   Vilfan ID, Lipfert J, Koster DA, Lemay SG, & Dekker NH (2009) Magnetic Tweezers for Single-Molecule Experiments. *Handbook of Single-Molecule Biophysics*, eds Hinterdorfer P & van Oijen A (Springer).
7.   Gosse C & Croquette V (2002) Magnetic tweezers: micromanipulation and force measurement at the molecular level. *Biophysical Journal* 82(6):3314-3329.
8.   Strick TR, Allemand JF, Bensimon D, Bensimon A, & Croquette V (1996) The elasticity of a single supercoiled DNA molecule. *Science* 271(5257):1835-1837.
9.   Wong WP & Halvorsen K (2006) The effect of integration time on fluctuation measurements: calibrating an optical trap in the presence of motion blur. *Opt Express* 14(25):12517-12531.
10.   te Velthuis A, Kerssemakers JWJ, Lipfert J, & Dekker NH (2010) Quantitative Guidelines for Force Calibration through Spectral Analysis of Magnetic Tweezers Data. *Biophysical Journal* 99(4):1292-1302.
11.   Lansdorp BM & Saleh OA (2012) Power spectrum and Allan variance methods for calibrating single-molecule video-tracking instruments. *Rev Sci Instrum* 83(2):025115.
12.   Kruithof M, Chien F, de Jager M, & van Noort J (2008) Subpiconewton dynamic force spectroscopy using magnetic tweezers. *Biophysical Journal* 94(6):2343-2348.
13.   Lipfert J, Kerssemakers JW, Jager T, & Dekker NH (2010) Magnetic torque tweezers: measuring torsional stiffness in DNA and RecA-DNA filaments. *Nat Methods* 7(12):977-980.
14.   Janssen XJ*, et al.* (2012) Electromagnetic torque tweezers: a versatile approach for measurement of single-molecule twist and torque. *Nano Lett* 12(7):3634-3639.
15.   Celedon A*, et al.* (2009) Magnetic tweezers measurement of single molecule torque. *Nano Lett* 9(4):1720-1725.
16.   Lipfert J, Wiggin M, Kerssemakers JW, Pedaci F, & Dekker NH (2011) Freely orbiting magnetic tweezers to directly monitor changes in the twist of nucleic acids. *Nat Commun* 2:439.
17.   Kauert DJ, Kurth T, Liedl T, & Seidel R (2011) Direct mechanical measurements reveal the material properties of three-dimensional DNA origami. *Nano Lett* 11(12):5558-5563.

18. Nelson PC, Radosavljević M, & Bromberg S (2008) *Biological physics : energy, information, life* (W.H. Freeman and Co., New York) Updated 1st Ed pp xxvi, 630 p., [634] p. of plates.

19. Bustamante C, Marko JF, Siggia ED, & Smith S (1994) Entropic elasticity of lambda-phage DNA. *Science* 265(5178):1599-1600.

20. Vologodskii A (1994) DNA Extension Under the Action of an External Force. *Macromolecules* 27(20):5623-5625.

21. Marko JF & Siggia ED (1995) Stretching DNA. *Macromolecules* 28(26):8759-8770.

22. Abels JA, Moreno-Herrero F, van der Heijden T, Dekker C, & Dekker NH (2005) Single-molecule measurements of the persistence length of double-stranded RNA. *Biophysical Journal* 88(4):2737-2744.

23. Herrero-Galan E*, et al.* (2013) Mechanical identities of RNA and DNA double helices unveiled at the single-molecule level. *J Am Chem Soc* 135(1):122-131.

24. Bouchiat C*, et al.* (1999) Estimating the persistence length of a worm-like chain molecule from force-extension measurements. *Biophysical Journal* 76(1 Pt 1):409-413.

25. Odijk T (1995) Stiff Chains and Filaments Under Tension. *Macromolecules* 28(20):7016-7018.

26. Wang MD, Yin H, Landick R, Gelles J, & Block SM (1997) Stretching DNA with optical tweezers. *Biophys J* 72(3):1335-1346.

27. Baumann CG, Smith SB, Bloomfield VA, & Bustamante C (1997) Ionic effects on the elasticity of single DNA molecules. *Proc Natl Acad Sci U S A* 94(12):6185-6190.

28. Strick TR*, et al.* (2003) Stretching of macromolecules and proteins. *Rep. Prog. Phys.* 66(1):1-45.

29. Calugareanu G (1959) L'intégrale de Gauss et l'analyse des nœuds tridimensionnels. *Rev. Math. pures appl* 4(5).

30. Călugăreanu G (1961) Sur les classes d'isotopie des noeuds tridimensionnels et leurs invariants. *Czechoslovak Mathematical Journal* 11(4):588-625.

31. White JH (1969) SELF-LINKING AND GAUSS-INTEGRAL IN HIGHER DIMENSIONS. *Am. J. Math.* 91(3):693-&.

32. Bhattacharyya A, Murchie AI, & Lilley DM (1990) RNA bulges and the helical periodicity of double-stranded RNA. *Nature* 343(6257):484-487.

33. Bryant Z*, et al.* (2003) Structural transitions and elasticity from torque measurements on DNA. *Nature* 424(6946):338-341.

34. Forth S*, et al.* (2008) Abrupt buckling transition observed during the plectoneme formation of individual DNA molecules. *Phys Rev Lett* 100(14):148301.

35. Mosconi F, Allemand JF, Bensimon D, & Croquette V (2009) Measurement of the torque on a single stretched and twisted DNA using magnetic tweezers. *Phys Rev Lett* 102(7):078301.

36. Moroz JD & Nelson P (1998) Entropic elasticity of twist-storing polymers. *Macromolecules* 31(18):6333-6347.

37. Moroz JD & Nelson P (1997) Torsional directed walks, entropic elasticity, and DNA twist stiffness. *Proc Natl Acad Sci U S A* 94(26):14418-14422.

38.   Gore J (2005) *Single-molecule studies of DNA twist mechanics and gyrase mechanochemistry* (University of California, Berkeley).

39.   Marko JF & Siggia ED (1995) Statistical mechanics of supercoiled DNA. *Phys Rev E Stat Phys Plasmas Fluids Relat Interdiscip Topics* 52(3):2912-2938.

40.   Vologodskii AV & Marko JF (1997) Extension of torsionally stressed DNA by external force. *Biophys J* 73(1):123-132.

41.   Bouchiat C & Mezard M (1998) Elasticity Model of a Supercoiled DNA Molecule. *Phys Rev Lett* 80:1556-1559.

42.   Ubbink J & Odijk T (1999) Electrostatic-undulatory theory of plectonemically supercoiled DNA. *Biophys J* 76(5):2502-2519.

43.   Neukirch S (2004) Extracting DNA twist rigidity from experimental supercoiling data. *Phys Rev Lett* 93(19):198107.

44.   Clauvelin N, Audoly B, & Neukirch S (2008) Mechanical response of plectonemic DNA: An analytical solution. *Macromolecules* 41(12):4479-4483.

45.   Clauvelin N, Audoly B, & Neukirch S (2009) Elasticity and electrostatics of plectonemic DNA. *Biophys J* 96(9):3716-3723.

46.   Neukirch S & Marko JF (2011) Analytical description of extension, torque, and supercoiling radius of a stretched twisted DNA. *Phys Rev Lett* 106(13):138104.

47.   Marko JF & Neukirch S (2012) Competition between curls and plectonemes near the buckling transition of stretched supercoiled DNA. *Physical review* 85(1-1):011908.

48.   Tempestini A*, et al.* (2012) Magnetic tweezers measurements of the nanomechanical stability of DNA against denaturation at various conditions of pH and ionic strength. *Nucleic Acids Res*.

49.   Salerno D*, et al.* (2012) Single-molecule study of the DNA denaturation phase transition in the force-torsion space. *Phys Rev Lett* 109(11):118303.

50.   Marko JF (2007) Torque and dynamics of linking number relaxation in stretched supercoiled DNA. *Phys Rev E* 76(2 Pt 1):021926.

51.   Brutzer H, Luzzietti N, Klaue D, & Seidel R (2010) Energetics at the DNA supercoiling transition. *Biophys J* 98(7):1267-1276.

52.   Kamien RD, Lubensky TC, Nelson P, & Ohern CS (1997) Direct determination of DNA twist-stretch coupling. *Europhys Lett* 38(3):237-242.

53.   Gore J*, et al.* (2006) DNA overwinds when stretched. *Nature* 442(7104):836-839.

54.   Lionnet T, Joubaud S, Lavery R, Bensimon D, & Croquette V (2006) Wringing out DNA. *Phys Rev Lett* 96(17):178102.

55.   Marko JF (1997) Stretching must twist DNA. *Europhys Lett* 38(3):183-188.

56.   Cluzel P*, et al.* (1996) DNA: an extensible molecule. *Science* 271(5250):792-794.

57.   Mergell B, Ejtehadi MR, & Everaers R (2003) Modeling DNA structure, elasticity, and deformations at the base-pair level. *Physical review* 68(2 Pt 1):021911.

58.   Lankas F, Sponer J, Hobza P, & Langowski J (2000) Sequence-dependent elastic properties of DNA. *J Mol Biol* 299(3):695-709.

59.   Sheinin MY & Wang MD (2009) Twist-stretch coupling and phase transition during DNA supercoiling. *Phys Chem Chem Phys* 11(24):4800-4803.

60.   Olsen K & Bohr J (2011) The geometrical origin of the strain-twist coupling in double helices. *AIP Advances* 1(1):012108-012108-012107.

61. Wereszczynski J & Andricioaei I (2006) On structural transitions, thermodynamic equilibrium, and the phase diagram of DNA and RNA duplexes under torque and tension. *Proc Natl Acad Sci U S A* 103(44):16200-16205.

62. Lionnet T & Lankas F (2007) Sequence-dependent twist-stretch coupling in DNA. *Biophys J* 92(4):L30-32.

63. Kosikov KM, Gorin AA, Zhurkin VB, & Olson WK (1999) DNA stretching and compression: large-scale simulations of double helical structures. *J Mol Biol* 289(5):1301-1326.

64. Milne RK, Yeo GF, Madsen BW, & Edeson RO (1989) Estimation of single channel kinetic parameters from data subject to limited time resolution. *Biophys J* 55(4):673-676.

65. Diekmann S (1989) Definitions and Nomenclature of Nucleic-Acid Structure Parameters. *Journal of Molecular Biology* 205(4):787-791.

66. Olson WK, Gorin AA, Lu XJ, Hock LM, & Zhurkin VB (1998) DNA sequence-dependent deformability deduced from protein-DNA crystal complexes. *Proc Natl Acad Sci U S A* 95(19):11163-11168.

67. Lu XJ & Olson WK (2003) 3DNA: a software package for the analysis, rebuilding and visualization of three-dimensional nucleic acid structures. *Nucleic Acids Research* 31(17):5108-5121.

68. Arnott S, Fuller W, Hodgson A, & Prutton I (1968) Molecular conformations and structure transitions of RNA complementary helices and their possible biological significance. *Nature* 220(5167):561-564.

69. Gast FU & Hagerman PJ (1991) Electrophoretic and hydrodynamic properties of duplex ribonucleic acid molecules transcribed in vitro: evidence that A-tracts do not generate curvature in RNA. *Biochemistry* 30(17):4268-4277.

70. Shi X, Herschlag D, & Harbury PA (2013) Structural ensemble and microscopic elasticity of freely diffusing DNA by direct measurement of fluctuations. *Proc Natl Acad Sci U S A* 110(16):E1444-1451.

71. Britton LA, Olson WK, & Tobias I (2009) Two perspectives on the twist of DNA. *J Chem Phys* 131(24):245101.

72. Matsumoto A & Olson WK (2002) Sequence-dependent motions of DNA: a normal mode analysis at the base-pair level. *Biophysical Journal* 83(1):22-41.

73. Chou FC, Lipfert J, & Das R (2014) Blind predictions of DNA and RNA tweezers experiments with force and torque. *PLoS computational biology* 10(8):e1003756.

74. Olson WK, Colasanti AV, Czapla L, & Zheng G (2008) Insights into the Sequence-Dependent Macromolecular Properties of DNA from Base-Pair Level Modeling. *Coarse-graining of condensed phase and biomolecular systems*:205.

75. Wenner JR, Williams MC, Rouzina I, & Bloomfield VA (2002) Salt dependence of the elasticity and overstretching transition of single DNA molecules. *Biophys J* 82(6):3160-3169.

76. Smith SB, Cui Y, & Bustamante C (1996) Overstretching B-DNA: the elastic response of individual double-stranded and single-stranded DNA molecules. *Science* 271(5250):795-799.

77. Odijk T (1977) Polyelectrolytes Near the Rod Limit. *J. Polym. Sci. Pt. B-Polym. Phys.* 15(3):477-483.

78. Skolnick J & Fixman M (1977) Electrostatic Persistence Length of a Wormlike Polyelectrolyte. *Macromolecules* 10(5):944-948.

79. Barrat JL & Joanny JF (1993) Persistence Length of Polyelectrolyte Chains. *Europhys Lett* 24(5):333-338.

80. Williams MC, Wenner JR, Rouzina I, & Bloomfield VA (2001) Entropy and heat capacity of DNA melting from temperature dependence of single molecule stretching. *Biophys J* 80(4):1932-1939.

81. Rief M, Clausen-Schaumann H, & Gaub HE (1999) Sequence-dependent mechanics of single DNA molecules. *Nat Struct Biol* 6(4):346-349.

82. Williams MC, Wenner JR, Rouzina I, & Bloomfield VA (2001) Effect of pH on the overstretching transition of double-stranded DNA: evidence of force-induced DNA melting. *Biophys J* 80(2):874-881.

83. Shokri L, McCauley MJ, Rouzina I, & Williams MC (2008) DNA overstretching in the presence of glyoxal: structural evidence of force-induced DNA melting. *Biophys J* 95(3):1248-1255.

84. van Mameren J*, et al.* (2009) Unraveling the structure of DNA during overstretching by using multicolor, single-molecule fluorescence imaging. *Proc Natl Acad Sci U S A* 106(43):18231-18236.

85. Gross P*, et al.* (2011) Quantifying how DNA stretches, melts and changes twist under tension. *Nature Physics* 7(9):731-736.

86. Fu H, Chen H, Marko JF, & Yan J (2010) Two distinct overstretched DNA states. *Nucleic Acids Res* 38(16):5594-5600.

87. Fu H*, et al.* (2011) Transition dynamics and selection of the distinct S-DNA and strand unpeeling modes of double helix overstretching. *Nucleic Acids Res* 39(8):3473-3481.

88. Zhang X, Chen H, Fu H, Doyle PS, & Yan J (2012) Two distinct overstretched DNA structures revealed by single-molecule thermodynamics measurements. *Proc Natl Acad Sci U S A* 109(21):8103-8108.

89. Bosaeus N*, et al.* (2012) Tension induces a base-paired overstretched DNA conformation. *Proc Natl Acad Sci U S A* 109(38):15179-15184.

90. King GA*, et al.* (2013) Revealing the competition between peeled ssDNA, melting bubbles, and S-DNA during DNA overstretching using fluorescence microscopy. *Proc Natl Acad Sci U S A* 110(10):3859-3864.

91. Léger JF*, et al.* (1999) Structural Transitions of a Twisted and Stretched DNA Molecule. *Physical Review Letters* 83(5):1066-1069.

92. Paik DH & Perkins TT (2011) Overstretching DNA at 65 pN does not require peeling from free ends or nicks. *J Am Chem Soc* 133(10):3219-3221.

93. Bonin M*, et al.* (2002) Analysis of RNA flexibility by scanning force spectroscopy. *Nucleic Acids Res* 30(16):e81.

94. Allemand JF, Bensimon D, Lavery R, & Croquette V (1998) Stretched and overwound DNA forms a Pauling-like structure with exposed bases. *Proc Natl Acad Sci U S A* 95(24):14152-14157.

95. Sheinin MY, Forth S, Marko JF, & Wang MD (2011) Underwound DNA under tension: structure, elasticity, and sequence-dependent behaviors. *Phys Rev Lett* 107(10):108102.

96. Schopflin R, Brutzer H, Muller O, Seidel R, & Wedemann G (2012) Probing the elasticity of DNA on short length scales by modeling supercoiling under tension. *Biophys J* 103(2):323-330.
97. Daniels BC, Forth S, Sheinin MY, Wang MD, & Sethna JP (2009) Discontinuities at the DNA supercoiling transition. *Physical review* 80(4 Pt 1):040901.